Prostate Cancer Characterization at Ultra-high Field MRI

Mariska Luttje

Colophon

This manuscript has been written using the freely available LaTeX typesetting and text formatting system.

Prostate Cancer Characterization at Ultra-high Field MRI
PhD thesis, Utrecht University, the Netherlands

Copyright © Mariska Luttje, 2017
The copyrights of chapter 5 have been transferred to Wiley.

ISBN: 978-90-393-6774-2

Cover design: Adapted from BSGstudio
Printing: Ridderprint BV, the Netherlands

This research was accomplished with financial support of the Dutch Cancer Society.
Grant Number: UU -2009-4500.
Financial support for the publication of this thesis was generously provided by Philips.

Prostate Cancer Characterization at Ultra-high Field MRI

Karakterisering van prostaatkanker met behulp van ultra-hoog veld MRI

(met een samenvatting in het Nederlands)

Proefschrift

ter verkrijging van de graad van doctor aan de Universiteit Utrecht
op gezag van de rector magnificus, prof. dr. G.J. van der Zwaan,
ingevolge het besluit van het college voor promoties
in het openbaar te verdedigen
op donderdag 18 mei 2017 des ochtends te 10.30 uur

door

Mariska Petra Luttje

geboren op 20 oktober 1986
te Enschede

Promotoren: Prof. dr. P.R. Luijten
Prof. dr. U.A. van der Heide

Copromotor: Dr. ing. D.W.J. Klomp

Vouloir, c'est pouvoir
Waar een wil is, is een weg

Voor mijn ouders, Pieter en Gerdien

Contents

1	General Introduction and Thesis Outline	1
2	Comparison Intrinsic SNR: 3T vs 7T	11
3	R2* Imaging of the Prostate at 3 and 7T	25
4	^{1}H MRSI in the Prostate at 7T	37
5	Combined ^{1}H/^{31}P MRSI in the Prostate at 7T	53
6	General Discussion and Summary	65
7	References	74
8	Addenda	85

“Fais toujours de ton mieux même
si personne ne regarde”

1 General Introduction and Thesis Outline

1

Prostate Cancer

Prostate cancer is the most frequently diagnosed cancer among European and American men [1, 2]. Prostate cancer is commonly diagnosed in middle aged to elderly men, with a risk of 1 out of 7 during lifetime [2]. A prostate-specific antigen (PSA) blood test is often used by the general practitioner as the first diagnostic tool for prostate cancer. Due to the rising age of the population and the increasing number of PSA blood tests, the incidence of prostate cancer is increasing [3, 4]. In the Netherlands, more than 10,000 men are diagnosed with prostate cancer yearly (IKNL), while prostate cancer is the cause of death of approximately 2,500 men per year. It can be stated that most of the men die with, rather than due to prostate cancer due to its often unaggressive nature. This form of overdiagnosis leads to overtreatment of prostate cancer resulting in reduced quality of life that could have been prevented with better diagnosis [4].

Anatomy & Pathophysiology

The prostate gland is a part of the male reproductive system located in the pelvis. The size varies from man to man, with an average of around 30-40ml. The prostate surrounds the base of the bladder with 2 lobes surrounding the urethra. Roughly, the prostate is built up from glandular epithelial cells producing the fluid portion of the semen, muscle cells controlling the urine flow and ejaculation and fibrous cells in the capsule of the prostate. Three different anatomical zones can be distinguished; the peripheral zone, central zone and transition zone based on their embryologic source. The peripheral zone is located closest to the rectum; around 75% of the prostate tumor are located here [5]. The transition and central zone enlarge over age, which is called benign hyperplasia (BPH). Most of the prostate tumors are adenocarcinomas (95%), the other 5% is thought to arise from the urothelial lining of the prostatic urethra.

In 1966 ,the pathologist Donald Gleason developed a grading system for prostatic adenocarcinoma which has been embraced globally [6].The Gleason score has been adapted over time and is based on a microscopic assessment of the cancer architecture ex vivo [5]. It is composed of a scoring system (up to grade 5), adding the two most common grades seen in a histologic sample. Where a (summed) Gleason score of 8 or higher is considered high grade prostate cancer.

Current clinical practice for diagnosing prostate cancer

Whereas general practitioners only have two diagnostic means at hand, the PSA blood test and a digital rectal examination (DRE), urologists have a broader choice including biopsies guided by transrectal ultrasound (TRUS).

1

Prostate-specific antigen blood test

A prostate-specific antigen (PSA) test measures the concentration in blood of this protease in nanograms per milliliter (ng/mL). It is used for screening purposes and is shown to be useful in early detection of prostate cancer [3]. This protease is produced by the epithelia of the prostate. In healthy men, the PSA will be contained in the prostate gland, resulting in a low PSA level in blood. In prostate diseases, e.g. prostate cancer and prostatitis, the PSA level in the blood can rise due to disruptions of the glandular structure of the prostate. As PSA may potentially rise for benign tissue as well, the specificity of the test for prostate cancer is low. In the Netherlands, a threshold value of 3.0 ng/mL is being used to refer men for further examination. The use of this test for screening purposes remains controversial as the specificity is low and the outcome of the test does not reflect cancer aggressiveness [4].

Digital rectal examination

The digital rectal examination is commonly used for prostate cancer screening in which only the part of the prostate near the rectum can be investigated. A healthy prostate is considered to feel smooth and symmetrical, whereas prostate cancer tends to result in asymmetry and hard lumps. The DRE has a low sensitivity and specificity for the detection of prostate cancer [7].

Transrectal ultrasound guided biopsies

Men referred after a suspected DRE or blood test are often followed up with biopsies obtained under transrectal ultrasound guidance. As prostate tumors are not visualized well by ultrasound, a standard systematic approach for biopsies is being used. Using this approach 8 to 12 biopsies are taken mostly from the peripheral zone of the prostate. This results in not only an estimated underdetection of 20%, due to sampling errors, but also in around 50% of the cases in an underestimation of aggressiveness [8,9]. In case of negative biopsy results and a prolonged suspicion of prostate cancer, a second round of biopsies or an MRI of the prostate is indicated. Currently, Gleason scores acquired by biopsies or radical prostatectomy are the gold standard in diagnosing prostate cancer. However, due to the sampling errors and its invasive nature, research is needed for more sensitive and non-invasive methods to detect and grade prostate cancer.

Multiparametric MRI

Because of its high soft-tissue contrast and high resolution, MRI provides the best visualization of the prostate compared to other imaging methods. The first use of MRI in the prostate was in 1983 at 0.35 tesla (T) [10]. Over time the field strength of MRI

has increased up to 3T for standard clinical practice. After the use of only anatomical scans for several decades, more and more functional scans are being used for the detection of prostate cancer, resulting in the nowadays commonly used multiparametric examinations. A multiparametric MRI (mpMRI) examination not only includes the conventional anatomical imaging with T2-weighed sequences, but also includes functional imaging e.g. diffusion weighted imaging (DWI), dynamic contrast enhanced imaging (DCE) and/or MR spectroscopy (MRS). Currently, the PI-RADS v2 is used to score lesions observed in the multiparametic examination [11, 12]. This is a 5-point assessment scale indicating the probability that mpMRI findings correlate with the presence of clinically significant prostate cancer at a particular location [12].

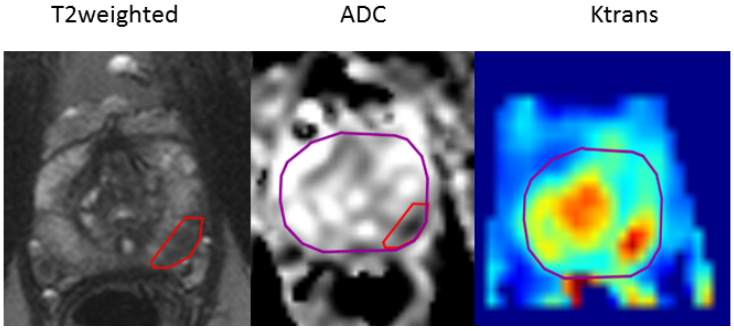

Figure 1.1: Tumor delineation at 3 tesla. A) T_2-weighted and B) ADC image, the tumor area is hypointense. C) Ktrans images calculated from the DCE examination, showing a hotspot in the tumor area and a false positive hotspot due to BPH in the transition zone. Adapted from chapter 4.

T_2-weighted imaging

Using T_2-weighted sequences high spatial resolution images can be acquired which clearly show the zonal anatomy of the prostate. Prostate tumors can be observed as low-intensity regions, most often observed in the peripheral zone. In the transition and central zone tumors are harder to localize in T_2-weighted imaging as BPH can both increase and decrease signal intensities in the prostate. Furthermore, false positive findings in the prostate can be due to prostatitis, scarring and post-biopsy hemorrhages.

T_1-weighted imaging

T_1-weighted images of the prostate are commonly used to detect post-biopsy hemorrhages to reduce the amount of false positive findings in T_2-weighted and DCE imaging.

Diffusion weighted imaging

Diffusion weighted imaging reflects the amount of water diffusion in the prostate as it exploits the relative differences in random restricted motion of water molecules within tissue. As the cellularity is increased in cancerous areas, diffusion is restricted. Therefore, the apparent diffusion coefficient (ADC), reflecting the diffusivity of water, is lower in tumors than in healthy tissue. The ADC can be derived from images acquired with a different 'b-value', reflecting different magnetic gradient strengths. While ADC correlates with Gleason scores, the confidence intervals largely overlap [13–15]. Sensitivity and specificity of DWI in prostate cancer are reported as high as 76% and 86% respectively [16]. The lack of anatomical detail and potential image artifacts due to magnetic susceptibility effects make it necessary to combine it with anatomical scans such as T_2-weighted images.

Dynamic contrast enhanced imaging

DCE MRI is widely used for cancer imaging in the human body. It consists of a series of fast ($<$10s) T_1-weighted gradient echo scans covering the prostate. Images are acquired before, during and after a bolus injection of a contrast agent such as gadolinium. Even though quantitative and semi-quantitative analysis methods exist, such as the Tofts model [17], radiologist often assess the images qualitatively for areas of early enhancement corresponding to a lesion on the T_2-weighted and ADC images. DCE has a high sensitivity for prostate cancer, however the low specificity hampers its usage as a single diagnostic scan especially for tumors in the transition zone, due to similar enhancement characteristics of BPH.

R2* imaging

Hypoxia is shown to be a predictive factor of oncologic outcome after radiotherapy [18, 19]. MRI might be able to give information on hypoxia in a non-invasive manner as hypoxia is related to the transverse relaxation rate R2* (1/T2*). Multiple studies show the correlation of R2* signal with hypoxia obtained in invasive needle electrode measurements and immunohistochemical staining [20, 21]. These studies suggest R2* imaging as a possible non-invasive method of determining tumor hypoxia status.

MR spectroscopy

Using MR spectroscopy spatially localized information about metabolites in the prostate can be acquired. The key metabolites observed in ^{1}H MR spectra of the prostate are total choline (tCho), polyamines (pa), creatine (cr) and citrate (cit). Changes in the choline metabolism are related to cancer malignancy [22, 23]. With ^{1}H MRSI the total choline and ethanolamine pool is measured, represented by tCho. The ratio between total choline

and citrate has been correlated to the presence of cancer [24, 25]. However, accurate measurement of the tCho/cit ratio is challenging, as the tCho peak at 3.2 ppm in ^{1}H MRS is close to polyamines at 3.1 ppm and creatine at 3.0 ppm. Therefore, the sum of all three metabolites is often considered instead of tCho only [26–28].

At higher field strengths like 7T the SNR gain and increased spectral resolution not only improve the separate detection of metabolites in ^{1}H MRS, but also opens the possibility of applying ^{31}P MRS. With phosphorus (^{31}P) MRSI, four individual compounds within the choline and ethanolamine pool can be detected: phosphocholine (PC), glycerophosphocholine (GPC), phosphoethanolamine (PE) and glycerophosphoethanolamine (GPE). PC and PE are involved in membrane formation, GPC and GPE in membrane breakdown. In various tumor types a switch of high GPC and low PC in benign cells to high PC and low GPC in malignant cells has been observed [29]. More recent, in vitro ^{31}P NMR measurements showed a significantly difference in PE and GPE (and their ratio) between cancer and benign prostatic hyperplasia [30].

Both ^{1}H MRS and ^{31}P are currently not applied in clinical MR routines amongst others due to the long acquisition time and the fact that there is no standardized automatic processing software yet. Nevertheless, both methods can be valuable to gain insight in the metabolism of the prostate, both in healthy and in malignant conditions.

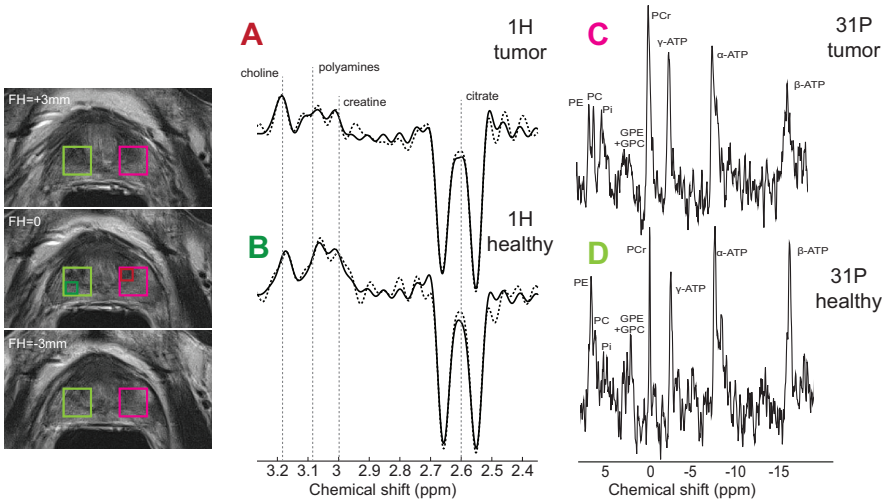

Figure 1.2: T_2-weighted image of the prostate indicating a healthy (green) and tumor (red) voxel. Please note that the ^{31}P voxel size is larger and therefore represented in 3 slices. A/B) ^{1}H MR spectrum of healthy and tumor area. C/D) ^{31}P MR spectrum of healthy and tumor area. Adapted from chapter 5.

1 Ultra-high field MRI

Ultra-high field MR systems (7T and above) provide both advantages and challenges compared to lower field strength systems. Advantages include a theoretical intrinsic SNR gain of more than two-fold and a higher spectral resolution. A higher SNR could be of clinical significance for diagnostic prostate imaging, for example when traded for higher resolution to detect or rule out extracapsular tumor extension. Furthermore, the higher spectral resolution gives rise to less overlap in prostate metabolites detected by ^{1}H MRS. The challenges, including increased tissue heating and reduced RF penetration depth, however can potentially diminish the advantages of 7T.

Outline of the thesis

Overdiagnosis and overtreatment of prostate cancer remain a major problem in patient care and health costs. Non-invasive diagnostic imaging tools are of specific interest to assess prostate cancer aggressiveness and help the therapy decision-making process. Non-aggressive lesions may be followed up by a watch-full waiting program, including yearly examinations of the prostate, whereas potentially life threatening lesions deserve immediate measures. Therefore, it is necessary to improve non-invasive tumor characterization methods for selective treatment of only those tumors which are potentially harmful.

Nowadays, MRI is increasingly used in clinical practice to detect the primary prostate tumor. However, in spite of the use of higher magnetic field strengths (up to 3T), the characterization of tumor aggressiveness remains limited. In this thesis, new methodologies using ultra-high field MRI have been developed and evaluated for the non-invasive assessment of prostate cancer aggressiveness.

In chapter 2, the SNR improvement at 7T in comparison to the clinically used 3T MRI is investigated. For that purpose a novel coil design containing 8 dipole antennas in combination with 16 loops is used at 7T, while 3T imaging was performed with a commercially available clinically used state-of-the-art 32-channel body array. The SNR improvement at ultra-high field is also studied in the following chapters to investigate the use of noninvasive MR techniques for detection of prostate cancer aggressiveness.

Chapter 3 describes the use of R2* or blood oxygen level dependent (BOLD) imaging to discriminate prostate tumors from healthy tissue at both 3T and 7T. MRI might be able to give information on hypoxia in a non-invasive manner as hypoxia is related to the transverse relaxation rate R2* (1/T2*). However, at low fields, R2* can be substantially biased by the T2 of tissue.

In chapter 4, the potential of ^{1}H MRSI in prostate cancer at 7T is investigated. Using the increased spectral resolution in combination with both the gain in SNR and the short echo time used, up to 7 metabolites can be distinctively detected in prostate spectroscopy

in vivo.

Next, in chapter 5 ^{31}P MRSI is added to the scan protocol by enabling a single patient exam, using a newly developed double tuned endorectal coil. This results in the possibility to study the choline metabolism in more detail. This could improve diagnostic sensitivity as the individual compounds of the choline pool may correlate better to tumor aggressiveness.

Finally, in chapter 6 the findings of the previous chapters are summarized and critically discussed, and set the frame to give recommendations for clinical implications and future research.

“N’en rêve pas, fais-le”

2 Comparison of intrinsic SNR for body imaging at 3T and 7T

This chapter is based on:
Luttje M.P., Voogt I.J., Hoogduin J.M., Luijten P.R., van den Berg C.A.T., Klomp D.W.J., Raaijmakers A.J.E.,
Comparison of intrinsic SNR for body imaging at 3T and 7T using an array of 8 fractionated dipole antennas and 16 loop coils.

2

Abstract

Purpose. To investigate the intrinsic signal-to-noise ratio (SNR) gain in body imaging at the higher field strength of 7T compared to 3T.

Materials and Methods. 6 healthy volunteers and one patient with prostate cancer were scanned at 3T and at 7T. For honest comparison, imaging was performed with RF coil arrays optimal for each field strength. For 7T imaging, a newly developed local transmit-receive array was used with 8 dipole transceivers combined with 16 loop receivers. 3T imaging was performed with a commercially available state-of-the-art 32-channel body array. Intrinsic SNR was determined incorporating negligible relaxation effects and after flip angle normalisation. At 7T ultra-high resolution T_2-weighted images were acquired using voxel sizes down to 0.35x0.35x2mm^3.

Results. At the prostate, an increase in intrinsic SNR of 2.1 fold (1.7 to 2.6) was measured at 7T in comparison to 3T for six volunteers with a wide range in body-mass-index (21 to 32). The enhanced SNR facilitated ultra-high resolution T_2-weighted MRI in one patient with excellent tissue contrast within the prostate gland.

Conclusions. We demonstrated that ultra-high resolution T_2-weighted imaging of the prostate is possible at 7 tesla without endorectal coil using the available SNR benefits of the higher field strength. When SAR is not limiting the sequence and relaxation effects are negligible, an average gain in available SNR of 2.1 fold was observed between 7T and 3T.

Introduction

Prostate cancer is one of the most common forms of cancer in men, affecting 1 out of 6 men during their lifetime [2]. Prostate cancer is often indolent and could be followed up by a watchful-waiting program when non-invasive imaging/characterization methods are available. Therefore, it is necessary to improve non-invasive tumor characterization methods for selective treatment of only those tumors which are potentially harmful and which have extracapsular extension [3].

Multiple studies have shown that multi-parametric prostate MRI at 1.5 and 3T is helpful in detecting, localizing and staging prostate cancer. However so far, good correlation with disease aggressiveness is insufficient to prevent potentially unnecessary treatment [13, 31–34]. More insight into tumor metabolism and aggressiveness could be obtained by using MR spectroscopy [35–37] and ultra-high resolution imaging for capsular extention [38], but for better results a higher signal-to-noise ratio (SNR) is needed. The SNR increases for prostate MR imaging by going from 1.5 to 3 tesla [39], and should increase further when going to 7 tesla systems.

Patient studies at 7T involving prostate cancer showed until now satisfactory results for T_2-weighted imaging compared to 3T [40] and the first results of ^{1}H and ^{31}P MRS [41–44] at 7T were published. Imaging at 7T is technically challenging owing to RF inhomogeneity, increased tissue heating and reduced RF field penetration. These challenges could potentially diminish the advantages of 7T. Though numerous studies have documented the use of custom-built external arrays dedicated to prostate imaging at 7T to obtain good T_2-weighted imaging [45–49], until now the superior imaging performance of 7T over 3T has not been demonstrated in terms of SNR. This, combined with the fact that the RF signals do not penetrate easily at 7T makes the community wary that imaging of deeply located structures within the body such as the prostate may not be beneficial at 7 tesla.

SNR comparisons over field strengths are challenging as they depend on a wide range of parameters. Relaxation time constants are different, causing sequence parameters like echo time and repetition time optimized for one field strength to be different for the other field strength. Moreover, the RF coil arrays that can be used will be different, and even if the identical coil geometry is used, the electromagnetic interaction with the body is completely different, causing an optimized array for one field to be sub optimal for the other. Next, the uniformity of excitation will be different between field strengths, causing different regions to provide flip angles that match better to the nominal angle than other regions. And finally, SAR may prohibit the use of optimized sequence parameters that can result in suboptimal scan efficiencies and thus SNR penalties.

One of the ways to minimize the number of parameters in comparing SNR over field strengths is to assess the intrinsic SNR difference. A proton density image acquisition with a relatively low flip angle, very short echo time and large repetition time can make

the effect of relaxation parameter differences between field strength negligible. The SNR in such images will have a linear relation to the actual flip angle, which can be corrected with an actual flip angle imaging (AFI) method. Moreover, the low flip angle and long TR will not be limited by SAR constraints, so can be applied uncompromised on all field strengths. By assuring SNR optimized signal combination of the receiver elements [50] incorporating noise correlations, the flip angle corrected proton density images between the two field strengths can be used to assess intrinsic SNR differences.

Here, we demonstrate that the design of a dipole transceive antenna array with a loop coil receive array at 7T substantially outperforms state of the art 3T MRI of the prostate. We compare intrinsic SNR (neglecting T1, T2 and SAR effects) and show comparisons to the 3T setup for 6 volunteers. Furthermore, to demonstrate utilization of the enhanced SNR with an external coil array, high-resolution T_2-weighted images were acquired in one patient with prostate cancer.

Materials and methods

This study was approved by the institutional review board and informed consent from all subjects was obtained.

Coil configuration and setup

For this study a newly developed 8-element transceiver array consisting of fractionated dipole antennas [48] was combined with a detunable 16-element receive only loop coil array, Figure 2.1. Under each antenna two oval shaped receive loops (long axis: 16cm, short axis 10cm) were positioned with mutual overlap. The antenna length is 28 cm with two meanders distributed evenly in each leg. The receive coil dimensions are based on the dipole size as well as the circumference of an average European adult. The ideal antenna to body distance was determined earlier by Raaijmakers et al. [48] at 2 cm. To reduce coupling of the receive loops to the antenna, while ensuring sufficient coupling to the human body a body-loop distance of 8mm was used with a Qul/Ql ratio of 7.33 (Qul=110, Ql=15). Detuning networks block the current inside the loops at two locations during transmit. A lattice balun was used to suppress common mode currents. Preamp decoupling was implemented to reduce inter-element coupling. Simultaneously, the preamp decoupling network in each receive loop (where the cable is connected) acts as a high impedance for induced currents in the loop, which in addition to detuning contributes to suppressing induced currents in the loop during transmit. Each antenna/two loop structure is one of eight separate elements that can be placed around the pelvis, abdomen or chest of the imaging subject.

Potential additional tissue heating because of the presence of the loop coils was evaluated by numerical simulations, Figure 2.2 (Sim4Life, ZMT, Zurich, Switzerland). As a

result of these simulations and assuming worst case phase settings may occur (resulting in maximum local SAR values) the resulting average power limit was set to 3 W per channel to abide the 20 W/kg SAR limit of the IEC guidelines for any phase setting. The described array was interfaced using an 8-channel Tx/Rx switch and receive interface box (MR Coils BV, Zaltbommel, the Netherlands) to an Achieva 7 tesla MR system (Philips Healthcare, Cleveland, USA). 3 tesla results were acquired on a Philips Achieva 3T system (Philips Healthcare, Best, the Netherlands), using the commercially available SENSE Coil with 32 elements (Philips Healthcare, Best, the Netherlands).

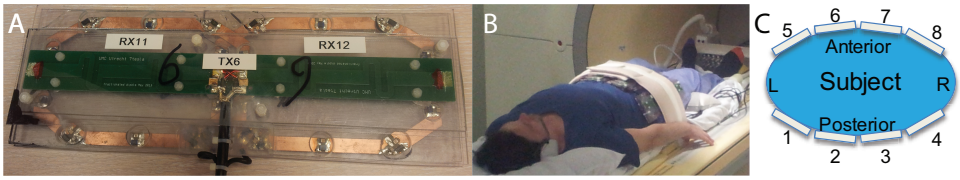

Figure 2.1: Experimental setup: (A) Under each antenna two oval shaped receive loops were positioned. To ensure spacing from the antenna towards the patient a 20 mm polycarbonate placeholder was designed in which the loops were at 8mm distance from the patient. (B,C) The 8-element array with receive loops was positioned in a belt-like fashion around the pelvis.

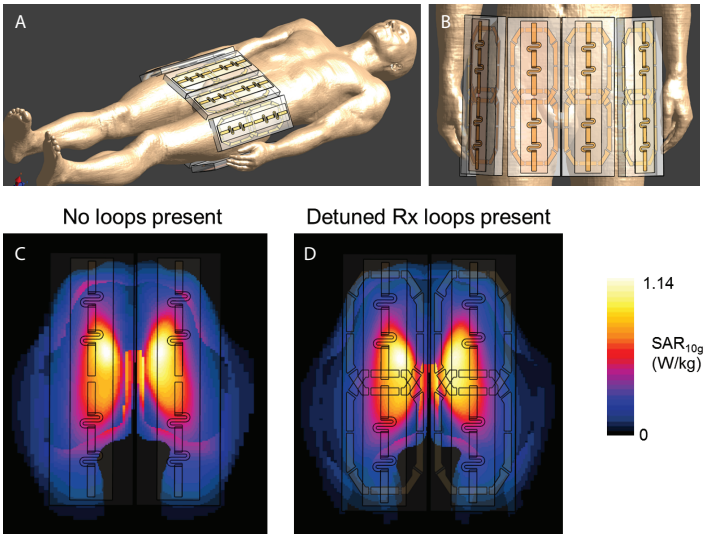

Figure 2.2: Safety was assessed by numerical simulations using the EM modeling package Sim4Life (ZMT, Zurich, Switzerland). The added receive loops are not influencing the local SAR levels compared to an antenna array only, which was proven to be safe for usage in earlier work [48]

.

MRI Acquisition volunteers

Six healthy volunteers (age: 24-56, BMI: 21.6-31.8) were included in this study. The healthy volunteer MRI protocol included at both 3T and 7T the following exams: A survey for localization purposes, B_1 shim series to optimize B_1 levels in the prostate, AFI B_1 map [51], T_2-weighted imaging for anatomical images and a proton density weighted gradient echo acquisition combined with a noise scan for SNR comparison. Noise correlation between the elements was measured using a noise prescan. The proton density gradient echo sequence was obtained using TR/TE=100/5 ms, a flip angle of 1°, FOV =250x430x25mm^3, voxel size= 2x2x2.5mm^3 and reconstruction voxel size = 1x1x1mm^3. The echo time (TE) was kept short to exclude T2 effects, while for T1 exclusion the repetition time (TR) was relatively long compared to the very low flip angle used. Noise correlation matrices of the array were acquired before each sequence.

MRI acquisition patient

One patient (62 years, PSA: 9.7 ng/ml) with biopsy-proven prostate cancer (Gleason score: 3+4 in 9/10 biopsies) was included in this study. Multi-parametric prostate MRI was performed using a 32 element torso/cardiac coil interfaced to a 3T MR scanner (Philips Ingenia, Best, the Netherlands). The T_2-weighted acquisition was acquired using the following parameters: TR/TE= 5900/100 ms, TSE factor=29, SENSE factor RL=1.5, FOV=200x200x90mm^3, voxel size= 0.78x0.78x3 mm^3 and reconstruction voxel size = 0.5x0.5x3mm^3.

At 7T, the protocol consisted of a survey for localization purposes, B_1 shim series to optimize B_1 levels in the prostate [26], AFI B_1 map [25] and one single slice T_2-weighted sequence (TR/TE=2500/90ms) with the same voxel parameters as the clinical 3T acquired sequence. In addition, this sequence has been repeated with higher resolutions (voxel size: 0.5x0.5x4mm^3, 0.5x0.5x2mm^3, 0.35x0.35x4mm^3 and 0.35x0.35x2mm^3) to explore the possibilities that the extra SNR provides.

MRI analysis

The acquired raw data of each element was reconstructed and combined in a processing step to achieve optimal SNR [50] using Matlab (Mathworks, Natrick, USA). The noise images from the elements were combined using the same phasing and weighting factors as determined for the corresponding proton density images. For each SNR measurement a rectangular region of interest (ROI) was delineated within the prostate mid-gland, after which the available SNR could be determined as the mean signal level in the ROI divided by the standard deviation of that same ROI in the noise image. Additionally the merit of the loops and antennas was investigated by reconstructing only from the raw data of either the loops or the antennas, followed by the SNR determination.

	coupling antenna-adjacent loop (dB)				coupling loop1-loop2 below corresponding antenna		coupling antenna-neighbour loop (dB)			
	tuned		detuned				tuned		detuned	
antenna	loop 1	loop 2	loop 1	loop 2	tuned	detuned	loop 1	loop 2	loop 1	loop 2
1	-14.5	-20.9	-19.7	-21.7	-16.0	-30.9	antenna 1 - left neighbour			
2	-19.4	-18.4	-22.8	-23.4	-17.5	-36.0	-16.3	-22.0	-32.7	-44.6
3	-26.9	-29.6	-23.9	-25.0	-13.7	-37.2	antenna 1 - right neighbour			
4	-9.8	-18.1	-15.5	-29.9	-16.6	-36.0	-23.0	-33.0	-43.0	-40.4
5	-13.1	-29.6	-21.9	-41.0	-16.0	-41.0	antenna 5 - left neighbour			
6	-12.9	-17.6	-18.6	-30.7	-16.0	-46.0	-30.2	-26.0	-38.7	-38.2
7	-15.4	-24.9	-23.6	-28.5	-15.9	-41.9	antenna 5 - right neighbour			
8	-15.9	-18.8	-21.9	-32.8	-13.5	-41.9	-24.0	-25.5	-42.0	-52.3

: Coupling levels between antenna and underlying loops, between two loops within one element and between antenna of one ele
loops of the neighbouring element.

Results

Coil array characterization

Noise correlation between coil array elements can potentially decrease the SNR in MR imaging. The noise correlation matrix of an array is therefore one of the indicators of an array's imaging performance. The noise correlation matrix is obtained for each volunteer at both 3T and 7T. A typical example of a matrix is shown in Figure 2.3. Due to their symmetrical placement, the loop coils and the dipole antenna are well decoupled (<-9.8dB without; <-15.5dB with detuning, Table 2.1). Noticeable is that the coupling between elements, particularly within the upper part and the lower part of the coil array at 3T is higher compared to any coupling between elements at 7T. Furthermore the noise correlation between neighbouring elements is less at 7T than at 3T, Figure 2.3.

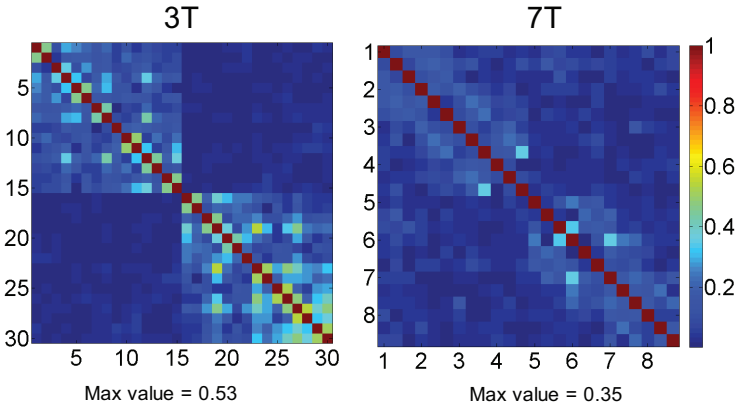

Figure 2.3: The noise correlation between neighbouring elements is less at 7T than at 3T, showing that the element decoupling in the 7T array is better than at 3T. At 7T, the numbered columns and rows represent the antennas, while the remaining correspond to the loops.

Volunteer	BMI	3T	7T	7T antennas	7T loops
#1	24.6	18.3	31.2	21.4	19.2
#2	22.4	23.0	48.8	21.0	36.6
#3	21.6	24.6	54.5	23.6	26.4
#4	25.8	21.1	41.6	31.4	31.6
#5	23.0	16.7	36.7	22.7	23.2
#6	31.8	15.1	36.8	25.6	20.4
Average SNR		19.8	41.6	24.3	26.2

Table 2.2: Measured SNR results at 3 and 7 tesla.

Available signal to noise ratio

6 volunteers with a varying age and body-mass-index (BMI) are scanned at both 3T and 7T consecutively. In Figure 2.4, the SNR maps of all six volunteers are shown for both 3 and 7T. The overview images show clearly the difference in signal homogeneity throughout the pelvis between 3 and 7T. When comparing the zoomed prostate images a difference in SNR in the prostate can be observed.

To determine the SNR in the prostate a rectangular ROI is delineated mid-gland with dimensions as large as the prostate size allows. At 3 tesla a mean SNR of 19.8±3.7 is obtained, at 7 tesla a mean SNR of 41.6±8.6 is measured in the same volunteers. This results in an average gain of available SNR of 2.1 fold in the prostate, Figure 2.5A and Table 2.2.

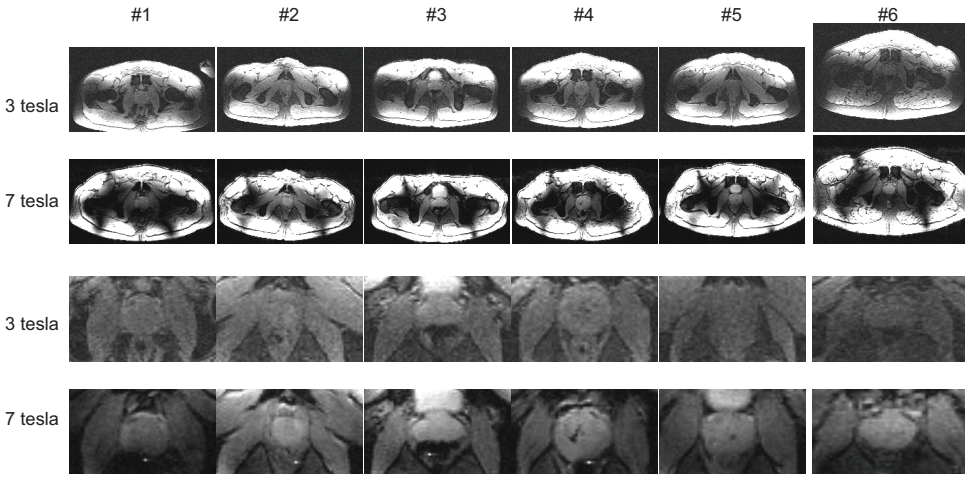

Figure 2.4: SNR maps of all 6 volunteers at 3 and 7T. In the overview images it can be clearly noticed that at 3T the pelvis is more homogeneous in signal intensity, while at 7T B_1 shimming was applied to create a homogenous signal in the prostate only. This can be seen in the zoomed images of 7T were the prostate has a higher signal intensity when compared to 3T. Furthermore the difference between the SNR at 3 and 7T is visible.

The contribution of the loops and antennas is measured by reconstructing the SNR measurement images using the raw data from either the loops or the antennas, Figure 2.5B. These results show that the 8 antennas and the 16 loops contribute equally to the SNR in the prostate. Since the noise correlation matrices show that there is no significant noise correlation between loops and antennas, and that their contribution in SNR is similar, the combination of loops and antennas should result in an SNR increase of approximately $\sqrt{2}$ ($+41\%$) in comparison to any of the two alone which is confirmed by the combined reconstruction.

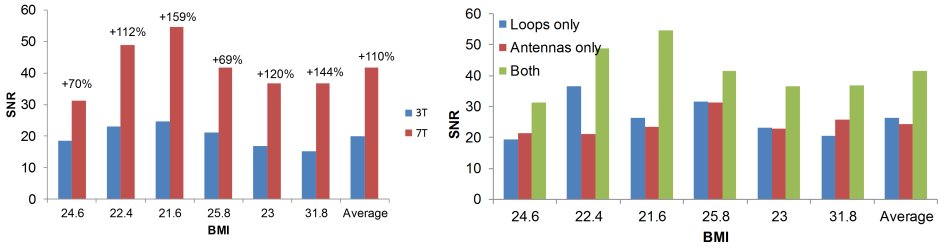

Figure 2.5: A) Bar diagram with results of the acquired SNR measurements at 3T and 7T per volunteer with BMI of the volunteers indicated. At 3 tesla an average SNR of 19.8±3.7 was obtained; at 7 tesla an average SNR of 41.6±8.6 was measured in the same volunteers. This results in an average gain in intrinsic SNR of 2.1-fold in the prostate. B) The contribution of the loops and antennas was measured by reconstructing the SNR measurement images with the raw data from either the loops only, the antennas only, or combined. This demonstrates an overall SNR gain of 40% when adding the receive loops to the antenna setup.

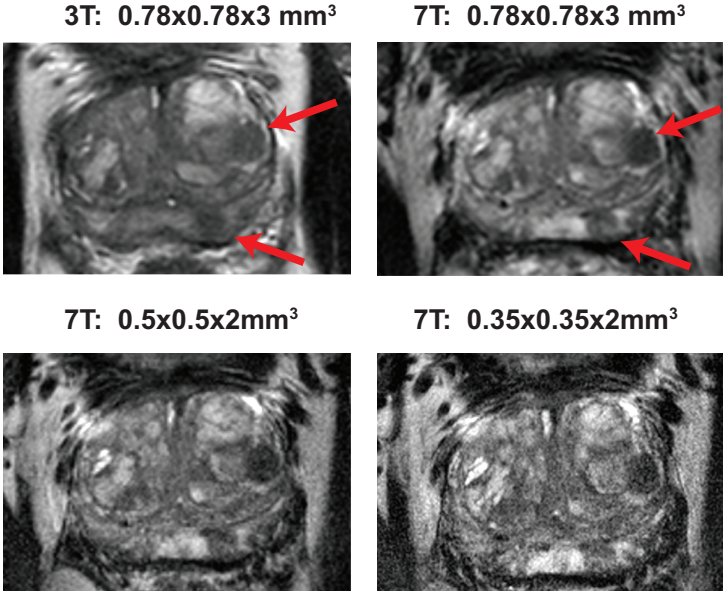

Figure 2.6: In this patient (62 years, PSA: 9.7 ng/ml) with biopsy-proven prostate cancer (Gleason score: 3+4 in 9/10 biopsies) two tumor areas are visible mid-prostate. Noticeable is the good T_2-weighted contrast between healthy and tumor areas at 7T. Anatomical details and contrast between healthy and tumor areas remain visible even at the resolution of 0.35x0.35x2mm^3 while clearly the SNR decreases.

High-resolution T_2-weighted imaging

In one prostate cancer patient (62 years, PSA: 9.7 ng/ml, Gleason score: 3+4) T_2-weighted images are acquired at 7T after the clinical 3T MR examination, both with external coils only. When comparing the clinical 3T examination to the 7T scan with the same resolution (Figure 2.6) it can be noticed that the 7T image is less noisy, furthermore an excellent contrast between tumor and healthy areas within the prostate gland can be obtained at 7T. Even when going to higher resolution T_2-weighted images, the noise levels stay low at 7T and the clear anatomical details remain, Figure 2.6.

Discussion

In this work, we demonstrated a more than 2-fold increase in available SNR in prostate MRI when comparing the use of an optimized coil array at 7T to a state-of-the-art coil array at 3T. Clinical prostate imaging is not only being used for diagnostic purposes, but also more and more for watchful-waiting purposes in patients with prostate cancer. A higher SNR is of clinical significance for diagnostic prostate imaging, for example because higher resolution is beneficial for detecting or ruling out extracapsular tumor extension. Furthermore, the gain in SNR may open up the possibility to detect the multifocal nature of prostate cancer better without the use of endorectal coils [31, 38, 52, 53]. Not only T_2-weighted imaging benefits from the higher SNR: MR spectroscopy, dynamic contrast enhanced sequences and diffusion weighted imaging are only a few of the prostate cancer characterization methods that can also profit from a higher SNR, while some of these simultaneously profit from an enhanced contrast mechanism at higher field strengths which comes on top of the SNR gain.

A few limitations of this study should be mentioned: Different coil setups are used at 3 and 7T, which may be considered a source of bias. However, a 3T vs 7T comparison with identical coils would favour one of the field strengths as optimal coil design depends on the field strength. In this study, the 7T coil array is an in-house developed array, while the 3T coil is a widely used, state of the art commercial coil and therefore considered an appropriate reference. Furthermore, no SENSE acceleration could be used at 7T due to software restrictions with this particular setup, which caused longer scan times. This resulted in suboptimal image quality of reconstructions at the scanner. To avoid potential bias, caused by the more sophisticated reconstruction methods available at 3T, images for both field strengths have been reconstructed from the raw data using the same algorithm. For fast acquisition a 1° flip angle was used for SNR determination, this could however potentially influence the resulting SNR due to inaccuracies in the B_1 maps. This inaccuracy is however multiple times smaller than the achieved gain in average SNR in the prostate.

At 7 tesla, approximately 3 minutes are needed to acquire the individual transmit

element field patterns and optimize the phase settings for constructive interference of the B_1 fields in the prostate (B_1 shimming). However, in overall developments, a short overall exam duration has not yet been targeted. The time delay for B_1 shimming can still easily be shortened with more optimized sequences and procedures. Furthermore, this delay can be compensated by faster imaging at 7 tesla due to the increased potential for parallel imaging at ultrahigh field strengths [54, 55] which is also reflected by the lower noise correlation matrices when compared to 3T, Figure 2.3.

In this study, where we explored the available SNR differences between 3T and 7T, we obtained the T_2-weighted MRI with only one slice to avoid any SAR violations. Currently, tools are being created to reduce the uncertainties in SAR levels between subjects and provide more accurate SAR assessments without the severe overestimations as used in this study. Also additional measures have been published to further reduce SAR levels [46,56].

The setup used in this study, using both loops and antennas, provided an overall gain of 2.1 fold in SNR compared to a commercially available coil with 32 elements at 3 tesla. Antennas are considered mainly suitable for higher frequencies like 7T [48] . However they may achieve improvements at 3 tesla as well. If implemented at 3T, it might improve image quality and thereby reduce the presented SNR improvement. On the other side, the coil arrays at 7 tesla are still heavily in development while the 3 tesla receive array is a fully engineered commercial product. If any, more improvement is expected for the 7T array than for the 3T array.

In conclusion, this study shows a new coil configuration with both antennas and loops in a surface coil array for prostate imaging at 7 tesla. Using this setup we demonstrated for the first time the benefits of the higher field strength of 7 tesla for prostate MR imaging using external elements only. Compared to a clinically used prostate imaging setup at 3 tesla, 7 tesla imaging resulted in an overall gain in SNR of 2.1 fold. Furthermore high resolution imaging was obtained at 7 tesla in one prostate cancer patient, to show the potential of going up to ultrahigh field prostate imaging with ultrahigh resolutions.

“Imaginer, c’est choisir”

JEAN GIONO

3 R2* Imaging of the Prostate at 3 and 7 tesla

This chapter is based on:
Luttje M.P., van Buuren L.D., van Vulpen M., van der Heide U.A., Klomp D.W.J., Towards intrinsic R2* imaging in the prostate at 3 and 7 tesla

3

Abstract

Purpose. Hypoxia is an important marker for resistance to therapy. In this study, we quantify the macroscopic effects of R2* mapping in prostate cancer patients incorporating susceptibility matching and field strengths effects

Materials and Methods. 91 patients were scanned without endorectal coil (ERC) at 3T. Only when rectal gas was absent, data was included for further analysis. Another group of 10 patients was scanned using a susceptibility matched ERC. To assess the residual contamination of R2 and macroscopic field non-uniformities, a group of 10 patients underwent an ultra-high resolution 7T MRI.

Results. Of the patients scanned at 3T 60% presented rectal gas and were excluded, due to susceptibility artefacts. At 3T the tumor was significantly different ($P<0.01$) from the healthy surrounding tissue in R2* values at intrapatient level. When using the measured median R2* value of $24.9s^{-1}$ at 3T and $43.2s^{-1}$ at 7T of the peripheral zone, the minimum contribution of macroscopic susceptibility effects is 15% at 3T.

Conclusions. R2* imaging might be a promising tool for hypoxia imaging, particularly when minimizing macroscopic susceptibility effects contaminating intrinsic R2* of tissue, such as rectal gas. At 3T macroscopic effects still contribute 15% in the R2* value, compared to ultra-high resolution R2* mapping at 7T.

Introduction

Hypoxia is shown to be a predictive factor of oncologic outcome after radiotherapy [18,19]. This makes hypoxia a potential marker for better selection of aggressive tumors and thereby improving anti-cancer therapy and radiotherapy planning. Unfortunately, hypoxia measurements are highly invasive and therefore not applicable in standard clinical practice. However, MRI might be able to give some information on hypoxia in a non-invasive manner as hypoxia is related to the transverse relaxation rate R2* (1/T2*) [20, 21]. Particularly at (ultra) high field strength (i.e. 3 and 7T) sensitivity to R2* is stronger than at lower field strengths (<1.5T) Also a higher discriminatorily between the R2 and R2* relaxation rates occur at high field strength.

R2* mapping of the prostate is feasible at 1.5T as has been shown in multiple studies [20, 21, 57]. R2* or blood oxygen level dependent (BOLD) imaging provides information about the oxygenation of tissue as the transverse relaxation rate (R2*) of water in blood and surrounding tissues increases due to the presence of endogenous paramagnetic deoxyhemoglobin. Previous studies show the correlation of R2* signal with invasive hypoxia measurements using needle electrode measurements and immunohistochemical staining [20,21,58]. These studies suggest R2* imaging as a possible non-invasive method of determining tumor hypoxia status. Furthermore an increase in tumor hypoxia using R2* mapping after androgen therapy has been shown [59]. The interpretation of these data is, however, under debate as other studies show opposite findings [60].

Measured R2* values are composed of intrinsic tissue relaxation ($R2^{*i}$), relaxations caused by macroscopic magnetic field non-uniformities ($R2^{+}$) and transverse relaxation rates (R2); $R2^{*} = R2^{*i}+R2^{+}+R2$. All of the studies mentioned above have been performed at the field strength of 1.5 tesla, where tumors are characterized by hypointense signals in T2 (1/R2) weighted MRI. At this field strength the difference between R2 and R2* values is relatively small, making the added value of T2* over T_2-weighted imaging questionable [20]. Moreover, while the BOLD effect is considered to affect the $R2^{*i}$ on the microscopic level, R2* imaging is very sensitive to macroscopic magnetic field non-uniformities as well. Partial volume effects may cause dephasing within the voxel caused by macroscopic susceptibility differences [61]. Particularly at air tissue interfaces macroscopic susceptibility effects can be substantial, similar as shown in BOLD imaging near the nasal cavity [62]. The rectum, which can contain rectal gas, is located in the proximity of the prostate and therefore is a potential origin of magnetic field non-uniformities, which increase the measured R2* values. Microscopic as well as macroscopic magnetic field non-uniformities scale both linearly with field strength, whereas R2 scales much less than linear. Therefore the measured R2* values at higher fields are less sensitive to alterations in R2. When the higher SNR at these higher field strengths is used to increase the spatial resolution, within-voxel dephasing will be reduced, making R2* imaging less sensitive to macroscopy field non-uniformities as well [63].

In this study, we investigated the feasibility of BOLD imaging at 3T and 7T in patients with prostate cancer. First, 91 patients were scanned without an endorectal coil (ERC), and only when rectal gas was absent in the MRI (34 patients), the data were included for further analysis. Next, another group of 10 patients was scanned using a susceptibility matched endorectal coil to exclude all potential air tissue interface effects, hence minimizing macroscopic magnetic field non-uniformities. Finally, to assess the residual contamination of R2 and macroscopic field non-uniformities in BOLD imaging, a group of 10 patients underwent an ultra-high resolution 7T MRI with a susceptibility matched endorectal coil.

3

Materials and methods

Study population

Ninety-one men with biopsy proven prostate cancer eligible for brachytherapy received a multiparametric prostate MRI, including R2* mapping, at the radiotherapy department before treatment planning. Patients receiving adjuvant hormonal therapy at the time of the MR scan were excluded. Of the 91 included patients at 3 tesla, seven were excluded: one because of unusable T_2-weighted imaging and six because no tumor was detected by MR imaging.

Another group of 10 patients was scanned at 3T using a susceptibility matched endorectal RF coil [64,65] to exclude potential air tissue interface effects on R2* values. To quantify the effects of remaining macroscopic susceptibility on the measured R2*, in yet another 10 patients a susceptibility matched endorectal RF coil was used at 7 tesla while increasing spatial resolution by almost an order of magnitude.

Informed consent was obtained from all patients scanned at 7 tesla, institutional review board (IRB) approval was waived for the usage of the multiparametric prostate scans obtained at 3 tesla.

Imaging

Multiparametric prostate MRI was performed using a 32 element torso coil interfaced to a 3T MR scanner (Philips Achieva, Cleveland, USA). Multiparametric prostate MRI consisted of T_1-weighted (T1w) using a balanced turbo field echo sequence (balanced TFE), T_2-weighted (T2w) MRI, diffusion weighted imaging (DWI), dynamic contrast enhanced MRI (DCE) and R2* MRI. The acquisition of T1w, T2w, DWI and DCE images were described in detail earlier, as well as the calculation of the apparent diffusion (ADC) and Ktrans values from the DCE images [17,66]. To obtain R2* maps at 3T a multi gradient echo (mGE) sequence (TR(ERC vs torso coil)/TE=73 or 77/5ms, ΔTE=6ms, echo train length=10, acquired voxel size=1.5x1.5x6.0mm^3, reconstructed voxel size = 1x1x3mm^3,

FOV= 280x400x75mm^3) was used. To further minimize the effect of air close to the prostate, a combination of a 6 element cardiac coil and an endorectal coil (MEDRAD, Pittsburgh, PA, USA) filled with either perfluoropolyether fluorinated or perfluorocarbon (PFC) fluid (GALDEN; Solvay Solexis, Milan, Italy) was used in 10 patients while using the same 3 tesla protocol. At 7 tesla (Philips Healthcare Best, The Netherlands) a two elements endorectal coil [44] (MR coils BV, Zaltbommel, the Netherlands) tuned and matched at 298 MHz was used and filled with fluorinated fluid (GALDEN, Solvay Solexis, Milan, Italy). Here an mGE sequence was obtained with parameters: TR/TE=78/2ms, ΔTE=4ms, echo train length=10, acquired voxel size=1.0x1.0x2.0mm^3, reconstructed voxel size=0.94x0.94x1mm^3, FOV=120x120x88mm^3.

R2* maps were calculated by fitting the signal of the mGE images using a least-squares approach in Matlab (v2012a, The MathWorks, Natick, MA) for both 3 and 7T data. Delineation of the whole prostate, peripheral and central zone was performed by using the guidelines of Villeirs et al. [67, 68] on the T2w and balanced-TFE scans. Delineation of tumor suspected volumes was based on hypointense values on the T2w, low ADC and high Ktrans values [11]. In a few patient cases the T2w imaging, ADC and Ktrans did not match due to e.g. patient movement; in these cases the T2w imaging and ADC map were deemed more important for delineation. To assure sufficient signal to noise ratio in the ultra-high resolution scans at 7 tesla, only the peripheral zone near the endorectal coil was delineated.

Analysis

The 84 patients examined at 3T without ERC were divided in two groups based on the visual presence of rectal gas (diameter<1cm) near the prostate on the 3 tesla mGE image. Areas with residual hemorrhage from biopsy on the T_1-weighted images were excluded from the analysis. Only when rectal gas was absent in the MRI, the data were included for further analysis. Interpatient differences between tumor suspected region and healthy surrounding tissue (i.e. peripheral, central zone or both) were analyzed for the group without visible rectal gas as well as for the 3T ERC group using the Friedman test as data was not normally distributed. For intrapatient statistics the Kruskal-Wallis test with a Dunn's posthoc test and Bonferroni correction was used. A p-value <0.05 was considered statistical significant. GraphPad Prism (GraphPad Software, San Diego, CA) was used for statistical analysis. The fraction of intrinsic R2* was estimated using the measured R2* data obtained from the peripheral zone at both field strengths. When we define, $R2^+_{3T}$ = a$R2^{*i}_{3T}$, $R2^+_{7T}$ = b$R2^{*i}_{7T}$, and use the linear field-dependence [69] for $R2^{*i}$ ($R2^{*i}_{7T}$ = 7/3*$R2^{*i}_{3T}$) then

$$(1+a)\ R2^{*i}_{3T} = R2^*_{3T}\text{-}R2_{3T} \quad (1)$$
$$(1+b)\ R2^{*i}_{7T} = R2^*_{7T}\text{-}R2_{7T} \quad (2)$$

$$\text{or } (1+a)/(1+b) = 7/3*(R2*_{3T} - R2_{3T})/(R2*_{7T}-R2_{7T}) \quad (3)$$

where a and b are the relative relaxation rates of macroscopic susceptibility effects compared to the intrinsic R2* at 3T and 7T respectively. By assuming susceptibility effects were negligible at 7T (b=0), the least susceptibility effect at 3T was calculated using $R2_{7T}$=$R2_{3T}$=7s^{-1} from literature [70, 71].

Results

Of the 84 patients scanned at 3 tesla without endorectal coil, 50 (60%) patients presented rectal gas and were excluded for further analysis, as the presence of rectal gas leads to susceptibility effects, Figure 3.1. Decay curves of patients scanned with and without ERC at 3T are shown in Figure 3.2. Only 34 (40%) patients did not have visible rectal gas in the region of interest, Table 3.1. In this group of 34 patients, no significant interpatient differences in measured R2* were found between the regions of interest, Table 3.2. The median values were, central zone 23.6s^{-1}, peripheral zone 24.9s^{-1} and tumor suspected regions 24.0 s^{-1}, Figure 3.3A and Table 3.2. However, intrapatient statistics show that in 27 of the 34 patients (79%) the tumor suspected region was significantly different (P<0.01) from the surrounding peripheral zone, showing either higher or lower R2* levels, and in 28 patients (82%) from the central zone, Table 3.3. Only in a few cases, we observed contrast between the tumor suspected region and healthy tissue by visual inspection.

Patient characteristics (n = 54)			
	Without ERC	With ERC	With ERC
	(3T, n = 34)	(3T, n = 10)	(7T, n = 10)
Age, median (range)	67.9 (55-81)	62.5 (47-74)	68.5 (52-77)
PSA, median (range)	9.1 (3.7-38.0)	6.5 (3.6-10.1)	9.6 (0.8-13.4)
Gleason score			
3+3	20	6	6
3+4	11	3	4
4+3	3		
4+4		1	

Table 3.1: Baseline characteristics of the patients included in the analysis.

	Without ERC (3T, n = 34)	With ERC (3T, n = 10)	With ERC (7T, n = 10)
Peripheral zone	24.9	27.9	43.2
Central zone	23.6	25.6	n/a
Tumor	24.0	24.3	n/a

Table 3.2: Overview of all obtained median R_2^* values (s^{-1}) at 3 and 7 tesla.

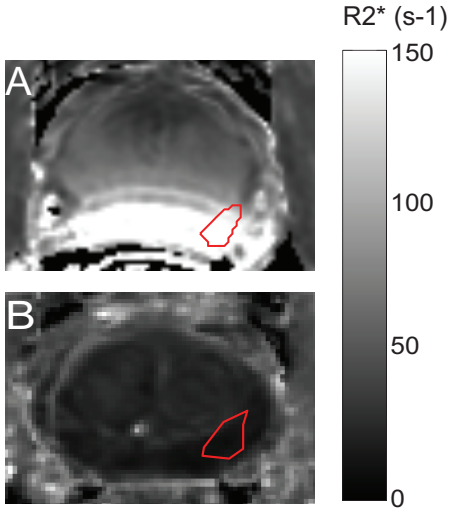

Figure 3.1: R2* maps of a patient with (A) and a patient without (B) rectal gas in the proximity of the prostate acquired at 3 tesla. The artificial increase in R2* near the rectal gas pocket (A) is substantial and cannot be attributed to hypoxia. In the other patient the R2* map of the prostate is more homogenous (B). The tumor locations in the peripheral zone are delineated in red.

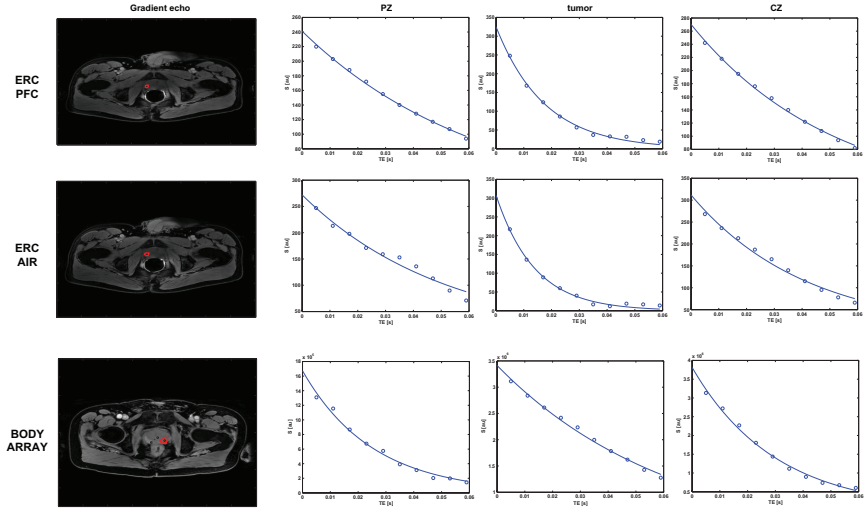

Figure 3.2: Decay curves of voxels in the peripheral zone, tumor and central zone of one patient scanned with an ERC filled with PFC or air and a patient scanned with a body array.

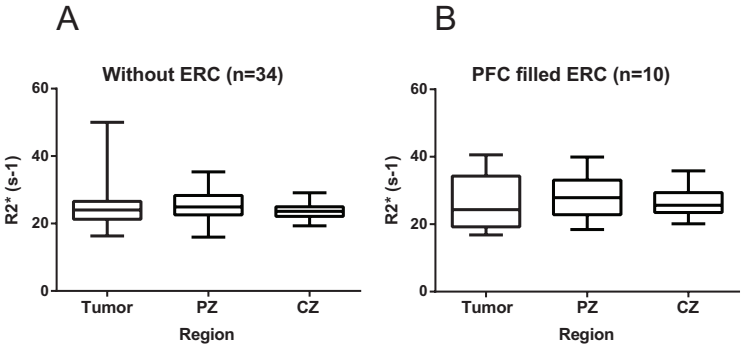

Figure 3.3: Box plots showing the R2* values in the different regions for the two subgroups; left, without rectal gas without endorectal coil; right, with endorectal coil filled with PFC at 3 tesla. No significant interpatient differences between the regions of interest were found for both patient groups.

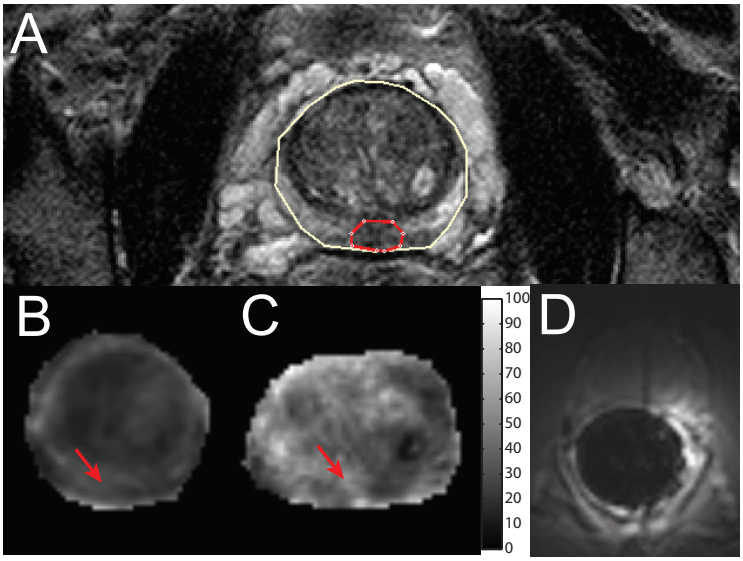

Figure 3.4: Patient without observed rectal gas, scanned at 3 and 7 tesla. A) T2w image at 3T of the same slice as the R2* maps. B) R2* map of the prostate at 3 tesla. C) High resolution R2* map of a slice at 7 tesla obtained with a susceptibility matched endorectal RF coil to minimize macroscopic susceptibility effects in measured R2*.D) Gradient echo image of the prostate at 7 tesla showing the limited field of view of the endorectal coil. Due to the use of an endorectal coil the prostate is deformed compared to the 3 tesla scans. Tumor locations are delineated in red or pointed out by an arrow.

Usage of a PFC filled endorectal coil at 3 tesla in 10 patients resulted in median R2* values of 25.6s^{-1} (central zone), 27.9 s^{-1} (peripheral zone) and in the tumor suspected region 24.3s^{-1}, Figure 3.3B and Table 3.2. No interpatient statistical differences were found between the regions of interest (P>0.05). Furthermore there was no significant difference between the values obtained in the patients without rectal gas and the patients scanned using a susceptibility matched filled endorectal coil (P>0.05). In the 10 patients scanned at 7 tesla a median R2* value of 43.2s^{-1} was detected in the peripheral zone near the PFC filled ERC, Figure 3.4. When using the measured R2* value of 24.9s^{-1} at 3T and 43.2s^{-1} at 7T of the peripheral zone, the minimum contribution of macroscopic susceptibility effects can be calculated from (Formula 3) by setting b equal to 0: (1+a)/(1+b) = 7/3*(24.9 - 7)/(43.2-7) = 1.15. The estimated minimal contribution at 3T is 15%, Table 3.2.

Patient	Tumor			PZ			CZ		
	median	int q25	int q75	median	int q25	int q75	median	int q25	int q75
#1	50.04	34.58	64.20	35.34	26.75	48.30	21.90	18.09	26.24
#2	24.53	22.19	27.77	31.23	23.05	43.10	21.45	18.04	26.66
#3	21.61	19.95	24.38	24.78	21.25	31.20	23.57	20.90	27.29
#4	19.42	16.70	24.40	25.53	19.88	34.13	20.96	17.05	25.60
#5	23.54	20.99	26.80	24.55	18.10	31.08	24.28	19.62	29.29
#6	27.86	22.76	35.17	23.63	17.18	34.13	29.13	22.66	44.32
#7	25.84	21.14	38.35	28.89	20.78	40.11	27.45	23.67	34.22
#8	48.51	41.34	70.79	31.40	23.73	46.60	21.61	18.26	27.99
#9	20.07	17.86	23.58	21.91	18.33	29.15	24.71	19.90	32.93
#10	26.96	23.22	32.42	28.11	15.53	51.53	24.54	20.07	31.53
#11	21.06	17.88	23.44	23.15	20.02	30.43	21.44	18.90	24.75
#12	24.15	21.92	27.57	21.69	18.32	25.66	22.18	19.33	25.62
#13	22.80	21.01	24.05	23.60	20.34	29.30	21.42	18.75	24.23
#14	22.96	20.51	25.21	22.46	18.82	27.76	21.60	18.63	25.82
#15	27.42	24.65	32.69	30.43	22.94	47.01	26.26	21.17	34.99
#16	24.33	21.66	29.63	26.80	21.13	37.12	25.08	21.55	30.20
#17	27.23	23.43	31.87	25.87	22.38	30.36	28.73	24.09	37.04
#18	27.59	25.62	30.56	27.01	22.21	34.83	24.01	20.79	27.79
#19	16.34	14.30	18.00	20.80	16.63	25.36	23.28	20.77	26.22
#20	25.76	21.78	31.83	22.58	17.63	31.36	19.31	15.98	22.38
#21	34.25	28.23	41.27	30.65	24.97	39.11	23.51	21.00	27.44
#22	23.08	20.82	25.64	22.99	19.76	27.36	22.19	19.57	25.45
#23	21.36	17.84	24.43	24.80	19.69	31.95	24.93	20.03	32.26
#24	17.46	16.15	19.38	18.70	14.81	24.74	23.34	19.26	28.03
#25	26.12	22.39	32.91	26.68	21.81	34.76	24.88	21.45	31.09
#26	19.13	16.96	21.33	22.59	18.80	28.52	25.97	21.81	33.15
#27	25.97	22.03	32.01	19.19	15.42	23.94	24.57	21.07	29.43
#28	24.11	18.51	30.24	26.70	21.93	34.54	26.18	20.96	33.01
#29	21.86	19.33	25.03	30.05	22.90	39.05	23.02	18.72	29.16
#30	26.47	23.04	29.63	24.66	19.29	32.72	25.66	21.50	32.79
#31	23.94	21.58	27.06	25.95	21.64	33.78	23.50	20.34	27.44
#32	20.64	16.30	25.04	15.98	11.77	22.96	23.70	19.94	27.90
#33	20.00	18.21	22.66	25.09	19.67	34.32	23.89	19.88	29.62
#34	22.45	20.24	26.86	31.05	23.33	42.16	22.17	18.94	26.59
Median	24.03	21.08	27.32	24.94	19.95	33.25	23.64	19.99	28.01

Table 3.3: Median, first and third quartile values obtained from Tumor, PZ, and CZ regions for all patients scanned with an external coil at 3T.

Discussion

In this study, we investigated the feasibility of intrinsic R2* imaging of the prostate in a group of men eligible for brachytherapy at field strengths of 3 and 7 tesla.

Of the 84 patients scanned at 3 tesla 50 patients (60%) presented with rectal gas, which results in susceptibility artifacts and erroneously high R2* values in the proximity of the air tissue interface. Due to this well-known artifact, areas near the rectum might be wrongfully assigned as hypoxic. In the other 34 patients (40%) no artifacts due to rectal gas were recognized. In 27 of these 34 patients (85%) the tumor suspected region was significantly different in R2* from the surrounding healthy tissue. The tumor delineation used here is based on multiparametric prostate MRI, which might be an underestimation of the pathohistological tumor areas. As biopsies were performed before imaging, the global biopsy locations and corresponding Gleason score were compared to our tumor suspected region from the imaging parameters. At 7T no tumor delineations were made as no DCE and DWI sequences were used. However, as most of the tumors are located in the peripheral zone, it can be assumed that the estimations made here for the peripheral zone are also relevant for the tumor areas. A full prostate coverage can be obtained by adding a body array to the setup to allow for optimal anatomical and physiological imaging. In case of a follow-up study with an ERC only, a slight reduced spatial resolution will have to be applied to recover sufficient SNR further from the ERC in order to acquire a complete prostate coverage. In this study only patients with a lower grade Gleason score of 6 (3+3) or 7 (3+4, 4+3) were included. Higher grade tumors might be more hypoxic and they are expected to deviate more from the healthy surrounding tissue [72–74].

It can be noticed that the R2* values of the dataset excluding rectal gas without the endorectal coil are similar to the values obtained with the susceptibility matched endorectal coil. From this it can be stated that the perfluorated liquid in the endorectal coil matches well to the susceptibility of the surrounding tissue, this method was therefore also applied during R2* mapping at 7 tesla.

Other proposed techniques for reducing the effect of macroscopic field inhomogeneities include tuned pulse sequences (i.e. extra local or tuned gradients [75, 76]) and R2* fitting techniques which take the macroscopic susceptibility effects into consideration [77, 78]. Recently, a Gaussian Augmentation of the Mono-Exponential (GAME) decay model was used to optimize R2* fitting of the prostate, however field gradients remain an issue with this method [79]. Most of the techniques described above lengthen acquisitions times by either changes in the scan sequence due to extra gradients or by tuning the gradients to their optimal state. Fitting and recontruction techniques will lengthen scantime due to the need of extra acquisitions to determine field and relaxation maps to avoid for example local minima [80]. Furthermore methods to get rid of the rectal gas could be explored, as well as the standard usage of endorectal coils filled with PFC; a technique we used to investigate the potential improvement in R2* mapping of the prostate.

Alonzi et al. [57] report mean values at baseline and after three months of therapy for the tumor (16.59 and 23.41 s^{-1}), benign peripheral zone (14.09 and 19.66 s^{-1}) and benign central zone (10.35 and 13.73 s^{-1}) in 20 patients with Gleason grade 6-9 at 1.5 tesla, whereas Chopra et al. [20] report a mean R2* value of 17.6s^{-1} both at 1.5 tesla. The BOLD effect ($R2^{*i}$) should increase linearly for increasing field strengths [69]. The median R2* values from the group without rectal gas reported in our study show in most cases an increase of less than a factor of two (3T/1.5T) compared to previous studies. However, when comparing the R2* values of the maps obtained at the even higher field strength of 7T, we also find no estimated linearly increase of R2* values (43.2 at 7 tesla vs 24.9 s^{-1} at 3 tesla). This suggests that still a substantial fraction of the measured R2* value at 3T, even without the presence of rectal gas near the prostate, is caused by macroscopic susceptibility effects rather than intrinsic R2*. In fact, even when assuming no T2 reduction at all at higher fields (i.e. assuming a T2 of 142 ms (or R2 = 7s^{-1}) in the peripheral zone [70, 71]) and assuming negligible macroscopic susceptibility effects due to the higher spatial resolution at 7T versus 3T, the macroscopic susceptibility effect at 3T is still contributing at least 15% of the $R2^{*i}$ value on the measured R2* at 3T. Consequently, higher spatial resolutions that reduce dephasing in the voxels, stronger fields that expands R2* from R2, and susceptibility matching as demonstrated in this study resulted in R2* values closer to the intrinsic BOLD effect and thus pO2. Whether pO2 is sufficiently reflected by the measured R2* still needs to be assessed with hypoxia measurements, for example using oxygen electrode measurements or PET with a hypoxia seeking ligand [20, 81]. Previous studies show a correlation between BOLD and delta pO2 after breathing challenges [82–84]. Further in vivo studies should be conducted to investigate this effect in human prostate.

To conclude, R2* imaging might be a promising tool for hypoxia imaging, particularly when minimizing macroscopic susceptibility effects such as the presence of rectal gas. In 85% of the patients without gas pockets the tumor suspected region was significantly different from the surrounding healthy tissue. Yet, even in this group, macroscopic effects are still substantial, as demonstrated in comparison to ultra-high resolution R2* mapping at 7 tesla.

“Les chefs-d’oeuvre ne sont jamais
que des tentatives heureuses”

GEORGE SAND

4 ^{1}H MRSI in the Prostate at 7 tesla

This chapter is based on:
Luttje M.P., Arteaga de Castro, C.S., Luijten P.R., van Vulpen M., van der Heide U.A., Klomp D.W.J.,
Detecting levels of seven different metabolites in-vivo in human prostate cancer using the high spectral resolution at 7 tesla.

Abstract

Purpose. In this study, the potential of detecting seven different metabolites in the prostate of patients with prostate cancer is investigated at 7 tesla in vivo.
Materials and Methods. 7 tesla MRSI was performed in 15 patients with biopsy-proven prostate cancer. Imaging was performed both at 7 and 3 tesla to define abnormal versus normal appearing tissue. ^{1}H MRSI was acquired using adiabatic slice selective RF pulses with water and lipid suppression. The spectra were fitted using an LCModel based fitting algorithm. ROC and intra-patient analyses were obtained.
Results. Inter-patient statistics show that the ratio (tCho+PA+Cr)/Cit calculated from the abnormal appearing tissue, peripheral zone (PZ) and central zone (CZ) were significantly different from each other. Correlations between choline, polyamines and citrate concentrations were significant, showing an inverse proportional behaviour between choline and citrate. The metabolites with short T2 relaxations, scyllo-inositol, myo-inositol and glycine did not correlate with choline, creatine, polyamines nor citrate.
Conclusions. Our results at 7T demonstrate the ability to detect seven metabolites distinctively in the prostate. The metabolite ratio (tCho+PA+Cr)/Cit significantly discriminates abnormal tissue as observed on MRI with normal appearing tissue. An inverse correlation is observed between choline and citrate concentrations, while the metabolites with short T2 showed no correlations.

Introduction

Prostate cancer is the most frequently diagnosed cancer among European and American men [1, 2]. Although less lethal than other types of cancers, prostate cancer can be under or overtreated, leading in some cases to long term impairments, particularly when treated with radical prostatectomy. Prostate cancer is diagnosed clinically and ultrasound guided biopsies are obtained to determine Gleason scores. However, US guided biopsies are prone to sampling errors leading to up to more than 50% underestimation of the Gleason scores, thus missing significant tumors [8, 9]. MRI is increasingly being used in clinical practice, due to its increased specificity and sensitivity for the detection of prostate cancer. However, the characterization of tumor aggressiveness remains limited [11, 85].

^{1}H magnetic resonance spectroscopic imaging (MRSI) is another MR technique that enables the detection of prostate metabolites including total choline (tCho), polyamines (PA, predominantly spermine), creatine (Cr) and citrate (Cit). These metabolites can be detected non-invasively [24, 41, 86]. ^{1}H MRSI of the prostate has already proven to be useful for the detection and staging of prostate cancer using the tCho/Cit ratio as choline levels increase and citrate levels decrease in aggressive prostate tumors [35, 87, 88]. However, accurate measurement of the tCho/Cit ratio remains challenging, as the tCho peak is close to PA and Cr. As the coupled spin system of the polyamines provides broad spectral lines around 1.9 and 3.1 ppm, it cannot be fully separated from the tCho at 3.2 ppm at 1.5T and 3T [25, 28, 41, 89]. Therefore, the ratio of the sum of these compounds over citrate ((tCho+PA+Cr)/Cit) is usually considered [28, 35]. This ratio can significantly differentiate tumor from healthy tissue in the prostate. However, multiple studies show that the influence of polyamines in this ratio might disturb the discrimination between prostate cancer and healthy areas. Shukla-Dave et al. [28] qualitatively investigated the influence of the polyamines resonance on the metabolite ratio at 1.5 tesla. For 50 patients in 90% of the benign voxels, the PA peak was higher than tCho. Less than 1% of the benign voxels had no detectable PA compared to 11% in malignant voxels. Swanson et al. [90] and Giskeodegard et al. [91] have shown a significant decrease in the concentrations of polyamines and citrate when comparing high grade (Gleason score>7) to low grade (Gleason score<=6) tissue samples. Next to that, results of several studies even suggest that creatine levels decrease in tumor tissue as well [91, 92].

The use of higher magnetic field strengths, such as 7 tesla, enables better metabolite signal separation as a result of the increased spectral resolution. Therefore, better detection of some metabolites that overlap at lower field can be obtained. Consequently, the multiplet peak of PA resonant at 3.1 ppm becomes less broad causing no longer overlaps with the resonance of tCho at 3.2 ppm. In addition to the distinct detection of tCho, Cit, PA and Cr at 7T, other metabolites such as myo-inositol (mIns), scyllo-inositol (sIns) and glycine may be detected as well.These metabolites have all been related to (prostate) cancer aggressiveness in ex-vivo studies [90, 91, 93–95]. However, these larger molecules

have relatively short T2 relaxation and are commonly not observed in most MRSI studies at lower field strengths that use relatively long echo times [24, 25, 35, 88]. Fortunately, at 7T, the optimum echo time where the signal of the complex spin system of citrate is fully absorptive is much shorter (TE=56ms) compared to studies at lower fields (145ms at 3T, 120ms at 1.5T) [96–98]. Recent studies at 3T using dedicated low TE sequences have indeed demonstrated the detection of mIns, sIns, and glycine [99–101].

In this study, the potential of detecting tCho, PA, Cr, Cit, myo-inositol, scyllo-inositol, and glycine at 7T in prostate cancer in vivo is investigated at short echo time. Moreover, the sensitivity of metabolite detection with MRSI at 7T is assessed for all metabolites. In addition, metabolite ratios are compared between the peripheral and central zones of the prostate are compared as well as areas that coincide with hypo-intensities observed on T_2-weighted MRI.

Materials and Methods

Phantom study

A cylindrical phantom was used to visualize the behavior of the polyamine signal at different field strengths using a short echo time single voxel sequence (STEAM, TE=11ms, TR=5s, voxel size=15x15x15mm^3, flip angle=90°). The phantom consisted of a mixture of prostate metabolites [27] and was measured in a dedicated volume coil at 1.5, 3.0 and 7.0 tesla (Philips, Best, the Netherlands).

Subjects

7 tesla MRI and MRSI of the prostate was performed in 15 patients with biopsy-proven prostate cancer after their clinical 3 tesla MR examination for radiotherapy planning. The mean age was 65 years (range: 51-71), mean PSA level 8.5ng/mL (range: 1.0-16.3) all with low grade (up to Gleason 7) tumors, Table 4.1. Written informed consent was obtained from all the patients participating in this study, which was approved by the local ethics review board.

Data Acquisition

A two-elements ^{1}H transmit and receive (TxRx) endorectal coil (ERC) (MR Coils BV, Zaltbommel, the Netherlands) [44] was interfaced to a whole body 7 tesla MR-scanner (Philips Healthcare, Best, the Netherlands). The inner balloon of the ERC was filled with fluorinated fluid (Galden, Solvay Solexis, Milan, Italy) to match the susceptibility of the ERC with the prostate, hence minimizing B0 shim artifacts. Gradient echo images (fast field echo (FFE), nominal flip angle= 45°, TR/TE=23/2 ms, FOV=500x500x3 mm^3) were

Patient	Age	PSA (ng/ml)	Gleason score
1	70	8.7	6 (3+3)
2	70	5.1	7 (3+4)
3	68	7.1	6 (3+3)
4	71	8.1	7 (3+4)
5	58	9.1	7 (3+4)
6	51	13.4	6 (3+3)
7	66	8.6	6 (3+3)
8	62	4.3	7 (3+4)
9	60	11.4	6 (3+3)
10	69	6.2	6 (3+3)
11	58	7.0	6 (3+3)
12	70	16.3	6 (3+3)
13	67	13.0	7 (3+4)
14	66	1.0	6 (3+3)
15	68	8.1	6 (3+3)

Table 4.1: Patient characteristics.

obtained for localization purposes. Anatomic information was acquired using T_2-weighted turbo spin echo (TSE) images (TR/TE=5000/74 ms, acquisition matrix 188x180, FOV= 150x150x58mm^3, 10 slices of 2 mm thickness) enabling the localization of the central and peripheral zone as well as abnormal tissue as identified on the 3 tesla MRI data. To enable second order image based shimming a B0 map (3D FFE, TR/TE1/TE2=5.2/3.0/4.0 ms, acquisition matrix 64x84, voxel size= 2.81x2.81x3 mm^3, 20 slices) was obtained. After B0 shimming the 2D ^{1}H MRSI grid was positioned through the hypo-intense (abnormal) area of the T_2-weighted MRI of the 7 tesla guided by the 3 tesla MRI data. ^{1}H 2D MRSI was acquired using adiabatic slice selective RF pulses in the anterior-posterior (AP) and feet-head (FH) directions with MEGA pulses [102, 103] for simultaneous water and lipid suppression and polyamine refocusing (nsLASER [98], TR/TE=2000/56ms, 24x8 matrix, nominal voxel size=5x5x5 mm^3, acquisition time=7.46 min).

Data processing

All MRSI voxels within the prostate were selected for each patient and used for the spectral analysis. Each voxel was manually inspected using the following exclusion criteria: insufficient signal to noise ratio (SNR <3), no splitting of citrate when present and the presence of strong lipid signals (>3-fold above the noise floor in the spectral region of interest).

Delineation of volumes of abnormal appearing tissue was based on relatively hypointense values on the T2w MRI, low ADC and high Ktrans values from the clinical performed 3 tesla scan. The 7 tesla results were blinded from any multi-parametric 3T MRI result. Voxels were assigned to be either in normal appearing peripheral zone (PZ), normal ap-

pearing central zone (CZ) or classified as abnormal (hypo-intensity) when more than 80% of the voxel was placed in such region; remaining voxels were excluded from further analyses.

Spectral fitting was performed using an LCModel based fitting routine [104] incorporating the ppm range of 2.2 to 3.85 ppm to include the metabolites of interest, while excluding the suppressed water and lipid signals. A basis set was created by simulations of citrate (Cit), creatine (Cr), spermine (PA), choline (tCho), myo-inositol (Mi), scyllo-inositol (Si) and glycine (Gly) using published values of chemical shifts and scalar couplings [33-35]. Peaks of choline (3.2 and 3.5 ppm), spermine (3.1), creatine (3.0 ppm), citrate (2.6 ppm), myo-inositol (3.52, 3.61 and 3.27 ppm), scyllo-inositol (3.3 ppm) and glycine (3.54 ppm) were fitted by the basis set using a varying phase, a variable but limited frequency offset ($\pm$4Hz) and linewidth in the 2.2 to 3.85 ppm range. The 1.9 ppm resonance of the polyamines was not included in the fitting routine as this resonance was suppressed by the lipid suppression scheme. Cramer-Rao lower bounds (CRLBs) were calculated for each metabolite per voxel.

After fitting, the following ratios were calculated for each voxel: (tCho+PA+Cr)/Cit, tCho/Cit and tCho/(Cit+PA+Cr). In addition, for each patient the metabolite ratios of each voxel were normalized to the median ratio in the normal appearing PZ of the patient for interpatient correlations. Correlations between the detected levels of myo-inositol, scyllo-inositol, glycine, choline, polyamides, creatine and citrate were investigated. Furthermore the fraction of these metabolite levels to the sum of all detected metabolite levels were calculated in each region of interest.

The Kruskal-Wallis test with Dunn posttest was used for inter-patient statistics to compare the calculated metabolite ratios in the different prostate areas, with and without normalization, where $P<0.05$ was considered statistically significant. Furthermore ROC analyses were performed and the areas under these curves (AUC) were calculated. Intra-patient statistics were performed on the non-normalized data using the Friedman test with Dunn posttest. All statistical analyses were obtained with GraphPad Prism 6 (San Diego, CA).

Results

At 7 tesla, the peak of the multiplet signal of PA resonating at 3.1 ppm no longer overlaps with the resonances of tCho and Cr as shown by the phantom study at different field strengths, Figure 4.1. While the identical phantom was used at all field strengths and obtained at short TE and long TR, the contribution of PA was substantially underestimated at the field strengths of 1.5 tesla and 3 tesla (see residual integrals in Figure 4.1), while the contribution of tCho and Cr were overestimated.

In all 15 patients total choline, polyamines, creatine and citrate could be detected. In

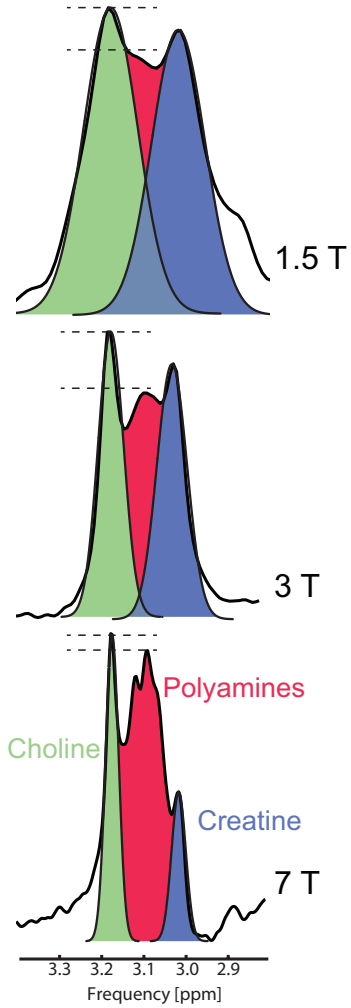

Figure 4.1: Spectra of a phantom of a mixture containing prostate metabolites measured at 1.5, 3.0 and 7.0 tesla using a short echo-time STEAM sequence. The J-coupled spin system of polyamines provides broad spectral lines, depending on the field strength. Noticeable is that the overlap of the polyamines by tCho and Cr is larger at 1.5T and 3T compared to 7T, which can lead to a substantial underestimation of the contribution of PA and overestimation of tCho and Cr at these field strengths.

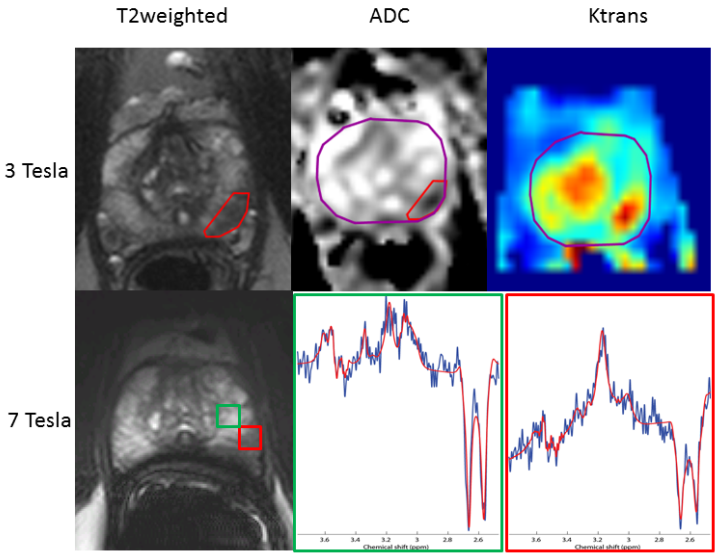

Figure 4.2: Abnormal area delineation at 3 and 7 tesla: A) T_2-weighted B) ADC C) Ktrans images from 3 tesla examination. D) T_2-weighted image of the same patient at 7 tesla with two highlighted spectra in the peripheral zone from inside (E) and outside (F) the abnormal region.

14 patients levels of scyllo-inositol, myo-inositol and glycine were also observed. After excluding the voxels with low MRS quality, the relatively high spectral resolution of all spectra from the remaining voxels facilitated distinctive fitting of the metabolites of interest. Delineation of abnormal appearing tissue volumes based on relatively hypo-intense values on the T2w MRI, low ADC and high Ktrans values from the clinical performed 3 tesla scan, are shown in Figure 4.2.

As one patient did not have any voxel containing at least 80% abnormal tissue in the T2w MRI, the data of this patient was removed from the analysis. Furthermore in one patient no scyllo-inositol, myo-inositol and glycine were detected. This resulted in 13 datasets containing 7 prostate metabolites and a total of 179 voxels that could be fitted using an LCModel based fitting routine, Figure 4.3 & 4.4. Note that in two patients the levels of polyamines were low in both abnormal and normal appearing intensity regions of the T_2-weighted MRI, Figure 4.5. One voxel that was close to the abnormal appearing area had been excluded from the peripheral zone group in patient 2. While the area was not delineated as abnormal, the ratio (tCho+PA+Cr)/Cit was very high in this voxel as it had no detectable level of citrate and therefore considered as outlier.

Cramer-Rao lower bounds (CRLBs) were calculated for each metabolite per voxel, resulting CRLBs lower than 20%, in 93% of the voxels for choline, 97% for citrate, 47% for glycine, 70% for myo-inositol, 47% for scyllo-inositol and 31% for the polyamines. CRLBs

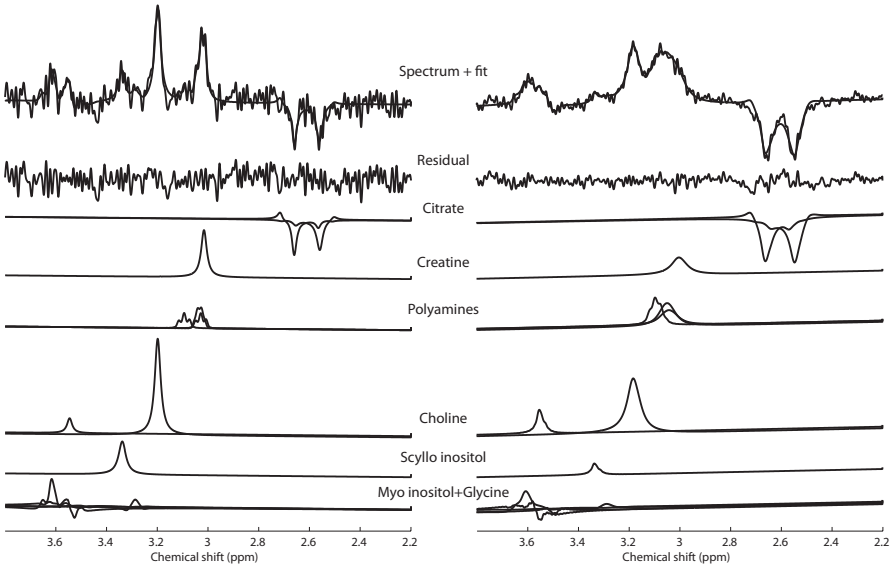

Figure 4.3: Example of basisset fitting of an two spectra of the prostate, showing all the fitted signals separately.

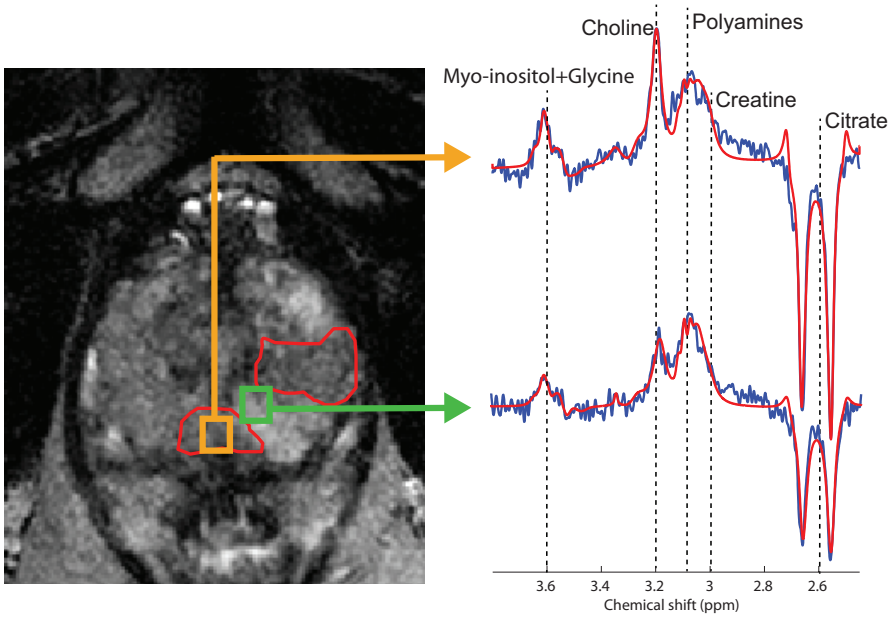

Figure 4.4: Example spectra (black) and results of the LC model basis set fitting (red) for patient 4. The orange box points out an abnormal region, while the green box indicates healthy appearing peripheral zone tissue. The changes in levels of choline and polyamines are clearly detectable.

above 40% were calculated in 3%, 2%, 28%, 7%, 32% and 37% respectively. CRLBs of creatine were in 94% of the voxels above 40%, resulting in unreliable fits.

Inter-patient statistics show that the ratio (tCho+PA+Cr)/Cit of the median values of the T2-hypo-intense areas vs. PZ and vs. CZ were significantly different from each other ($P<0.01$) while the median values of the PZ and CZ were not significantly different ($P>0.05$), Figure 4.6A. Using the newly proposed ratio tCho/(Cit+PA+Cr) no statistical difference was found between the regions of interest ($P=0.17$), Figure 4.6B. Whereas for the ratio tCho/Cit only the median values of the abnormal appearing tissue vs. PZ were statistically significant different ($P<0.05$), Figure 4.6C.

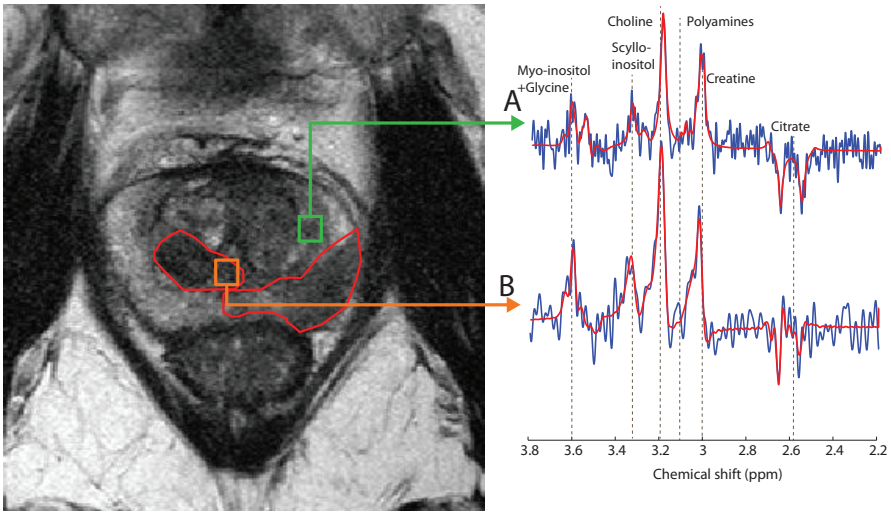

Figure 4.5: Example spectra obtained for patient 2 showing a general depression of the polyamines in the prostate. Spectrum A shows a voxel on the border of the healthy appearing central gland and peripheral zone. A typical tumor spectrum in this patient is shown in B; low citrate and polyamines, and elevated choline. In this patient also the scyllo and myo-inositol resonances were detected.

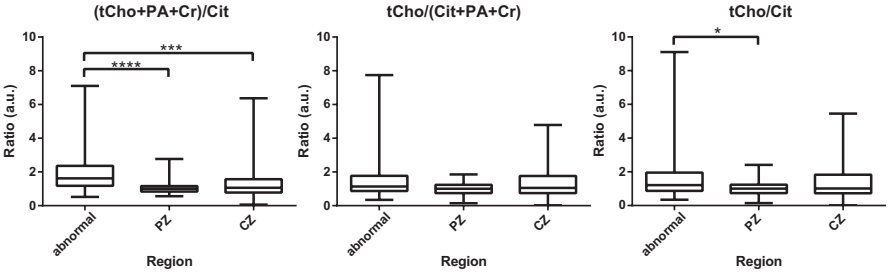

Figure 4.6: Inter-patient boxplots of the calculated metabolite ratios. The ratio (tCho+PA+Cr)/Cit differs from abnormal appearing tissue to either normal appearing peripheral zone ($p<0.0001$****) as well as normal appearing central zone ($p<0.01$***) being statistically significant in both cases.

Intra-patient statistics show that for the ratios (tCho+PA+Cr)/Cit and tCho/Cit the peripheral zone is significantly ($P<0.05$) different from the abnormal appearing tissue, Table 4.2 & 4.3. Furthermore using tCho/Cit the abnormal appearing tissue can be differentiated significantly ($P<0.05$) from the central zone. For the newly proposed ratio tCho/(Cit+PA+Cr) no significant differences were found for the regions of interest.

The metabolite ratios were further investigated by ROC analysis, Figure 4.7. This resulted in an AUC of 0.79 for the discrimination of hypo-intensity vs. PZ voxels and 0.70 for hypo-intensity vs. CZ voxels using the conventional ratio (tCho+PA+Cr)/Cit. For the ratio tCho/(Cit+PA+Cr) the AUC of abnormal appearing tissue vs. PZ was 0.60 and for abnormal appearing tissue vs. CZ 0.54 and 0.64 and 0.57 for the ratio tCho/Cit respectively. The metabolites with short T2 relaxations, scyllo-inositol, myo-inositol and glycine did not correlate with choline, creatine, polyamines nor citrate ($P>0.05$). Furthermore the fraction of these metabolites in the regions of interest was not significantly different, Figure 4.8.

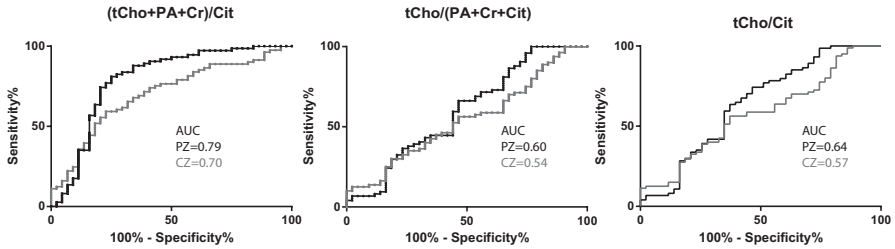

Figure 4.7: ROC curves showing the difference between the metabolite ratios. The AUC is reported as the area under the calculated ROC curve showing that the discrimination between abnormal appearing tissue and healthy appearing tissue is best for the ratio (tCho+PA+Cr)/Cit.

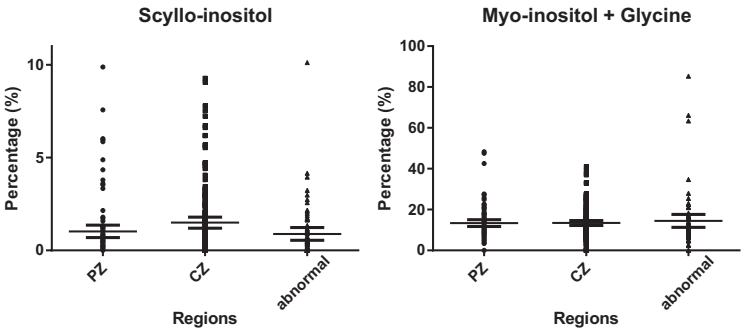

Figure 4.8: Fraction of scyllo-inositol and myo-inositol combined with glycine as part of all the metabolites detected in the regions of interest. No significant differences were found for tumor vs PZ.

	(tCho+PA+Cr)/Cit			tCho/(Cit+PA+Cr)			tCho/Cit		
Patient	CZ	PZ	Tumor	CZ	PZ	Tumor	CZ	PZ	Tumor
1	1.77	1	1.45	0.93	1	1.25	0.99	1	1.29
2	0.33	1	2.12	0.28	1	1.14	0.22	1	1.53
3	0.87	1	5.00	1.33	1	1.82	1.29	1	3.11
4		1	0.63		1	0.57		1	0.53
5	0.85	1	2.05	1.02	1	0.93	0.98	1	1.02
7	0.61	1	0.95	0.99	1	2.81	0.93	1	2.70
8	1.73	1	1.87	0.34	1	1.47	0.41	1	1.60
9	1.11	1	1.53	2.10	1	0.79	2.08	1	0.81
10	1.49	1	1.20	2.94	1	1.31	2.89	1	1.26
11	1.18	1	3.75	1.67	1	6.78	1.68	1	7.82
12	1.82	1	1.67	1.43	1	1.15	1.52	1	1.21
13	0.76	1	1.39	0.80	1	1.00	0.78	1	1.05
14	3.71	1	3.46	2.93	1	3.08	3.11	1	3.31
15	0.98	1	1.71	0.81	1	1.17	0.83	1	1.24

Table 4.2: Median ratios in regions of interest (NB: as all the data are normalized to the median ratio in the peripheral zone, the median peripheral zone ratio is 1).

	(tCho+PA+Cr)/Cit			tCho/(Cit+PA+Cr)			tCho/Cit		
Patient	CZ	PZ	Tumor	CZ	PZ	Tumor	CZ	PZ	Tumor
1	0.13	0.07	0.11	0.01	0.02	0.02	0.02	0.02	0.02
2	0.43	1.31	2.77	0.1	0.38	0.43	0.14	0.63	0.97
3	0.18	0.20	1.02	0.04	0.03	0.05	0.04	0.03	0.11
4		0.33	0.21		0.09	0.05		0.11	0.06
5	0.10	0.11	0.23	0.02	0.02	0.02	0.02	0.02	0.02
7	0.11	0.17	0.16	0.02	0.02	0.06	0.02	0.03	0.07
8	0.22	0.13	0.24	0.01	0.03	0.05	0.01	0.03	0.05
9	0.08	0.08	0.12	0.03	0.01	0.01	0.03	0.02	0.01
10	0.11	0.08	0.09	0.02	0.01	0.01	0.03	0.01	0.01
11	0.12	0.10	0.38	0.03	0.02	0.11	0.03	0.02	0.14
12	0.22	0.12	0.20	0.06	0.04	0.05	0.07	0.05	0.06
13	0.11	0.14	0.20	0.03	0.03	0.03	0.03	0.04	0.04
14	0.12	0.03	0.11	0.02	0.01	0.02	0.02	0.01	0.03
15	0.14	0.15	0.25	0.03	0.04	0.04	0.03	0.04	0.05

Table 4.3: Median ratios in regions of interest non normalized.

Discussion

In this study, individual fitting of the prostate metabolites was possible because of the high spectral resolution at the field strength of 7 tesla. This facilitated the investigation of the role of polyamines in ^{1}H MRSI of the prostate. Additionally the linewidth of the J-coupled spin system of polyamines is reduced from about 0.2 ppm at 3T to less than 0.1 ppm at 7T, assuming magnetic field non uniformities within the voxel remain lower than 0.1 ppm; a condition that was met for all of the 179 spectra. Therefore, in contrast to MRS obtained at lower fields, the 3.2 ppm resonance of choline could be distinctively detected from the resonances of polyamines at 3.1 ppm.

Similar as observed at lower field strengths, a significant difference in metabolite ratios was found between hypo-intense areas vs. PZ and CZ intensities as seen in T_2-weighted images using the conventional ratio (tCho+PA+Cr)/Cit. However, in contrast to our hypotheses, the placing of the polyamines in the denominator (tCho/(Cit+PA+Cr)) did not enhance the discriminating power of the ratio.

Our results do therefore not agree with the in vivo study of Garcia-Martin et al. [89] at 3 tesla that shows a significant difference for the ratio tCho/(Cit+PA) between PZ intensities (that corresponded to healthy tissue) and hypo-intense areas (that corresponded to presence of tumor). While for our study no histology validation of the abonormal appearing regions was available, their MRSI results did not match the histologic findings obtained from prostatectomy specimens, which may be due to the overlapping signals of PA with signals of tCho at 3T, which underestimates the PA. Ex vivo studies show that tCho increases and PA as well as Cit decrease in prostate cancer tissue [35, 87, 88]. A significant decrease in the concentrations of polyamines and citrate has been shown when comparing high grade (Gleason score>7) to low grade (Gleason score<=6) tissue samples [90, 91]. However, no data has been reported on the difference in polyamines levels between healthy and low grade tumor tissue, as was the case in our study.

In our current study, data of 14 patients with a relatively low Gleason score (3+3 and 3+4) were included. An overlap of the metabolite ratios between PZ intensities and abnormal appearing tissue was observed. The AUC of this ratio tCho/(Cit+PA+Cr) was lower than obtained by the conventional ratio where the polyamines are in the numerator.

A larger difference in the metabolic ratios between tumor and healthy tissue is expected for high Gleason grade prostate cancer caused by an increase of choline and a further reduction of the polyamines and citrate levels [91]. A successive study that incorporates registered histopathological data would be required to reveal the mechanism of the role of polyamine in the distinction of low grade versus high grade tumors. In addition to the distinct detection of tCho , Cit, PA and Cr at 7T, also metabolites with short T2 such as myo-inositol, scyllo-inositol and glycine can be detected as well. These metabolites with short T2 have been related to (prostate) cancer aggressiveness in ex-vivo studies [90, 91, 93–95, 105]. The standard spectroscopy sequences at lower fields do not allow

for quantification of these metabolites, however using 2D MRSI methods and short echo times the detection of these metabolites is possible. Previous prostate cancer studies in vitro (HRMAS) and in vivo (^{1}H MRSI) showed changes in myo-inositol and scyllo-inositol when comparing tumor tissue with healthy PZ [90, 91, 93–95]. The function of the inositols in the prostate is still mostly unknown even though myo-inositol has a relatively high concentration throughout the prostate [93, 94] which was observed in the current study as well.

Our study had several limitations. Firstly, the study group was small with 15 prostate cancer patients with Gleason scores 6 and 7. Nevertheless, we were able to obtain high quality spectra and statistically significant results when comparing the metabolic ratios calculated for the different areas in the prostate. A larger patient group with a higher range in Gleason scores in addition to the availability of histopathological information would be required to verify the discriminating power of the polyamines in more aggressive tumors. Secondly, MRSI data was obtained in only one slice of the prostate, while in studies at 1.5 and 3T the whole prostate is covered using 3D ^{1}H MRSI [24,25,35]. Extension to 3D MRSI can be feasible at 7T by incorporating reduced field of view encoding [42] or by applying echo planar readout trajectories [106]. So far we have used adiabatic RF pulses to obtain uniform excitation for ^{1}H MRSI and placed the CSI grid in only in the slice containing abnormal appearing tissue in the prostate due to limiting SAR constraints and acquisition times . Furthermore, the refocusing of the polyamines in the used nsLASER [98] sequence could lead to a more pronounced signal of polyamines compared to other studies. As this refocusing is performed by non-adiabatic MEGA (Mescher-Garwood) pulses the signal might not be uniform throughout the whole prostate due to the inherent decaying field with depth of the endorectal coil. This may be resolved using transmit coils with B1+ shimming techniques that lead to uniform transmit fields. Voxel wise classification can be improved by MR guided biopsies, MR-registered ultrasound guided biopsies or with registered whole mount pathology [107–109]. However, the indication for these invasive procedures differs between patients, and care must be taken not to bias the results to certain patient groups; i.e. by excluding patients where whole mount resections are not available as the primary treatment strategy is watchful waiting or radiation therapy.

In conclusion, in contrast to MRSI at lower field strengths, where polyamine signals overlap with choline signals and the echo times are relatively long, our results at 7T demonstrate the ability to detect seven metabolic resonances distinctively. This facilitated the investigation of the role of the individual metabolites in prostate when acquired with ^{1}H MRSI. When based on traditional imaging features to identify different intensity areas in the prostate, only the conventional metabolite ratio (tCho+PA+Cr)/Cit significantly discriminates between these regions at 7 tesla. Any combination of the seven metabolites had none or a less discriminating power at inter-patient level when compared to the traditional ratio so may be unique markers to grade the tumor.

“Ça ne se fera pas en un jour,
mais un jour, ça se fera.”

5 ^{31}P MRSI Combined with ^{1}H MRSI in the Prostate at 7T

This chapter is based on:

Luttje, M.P., Italiaander M.G.M., Arteaga de Castro C.S., van der Kemp W.J.M., Luijten P.R., van Vulpen M., van der Heide U.A., Klomp D.W.J., (2013).

^{31}P MRSI Combined with ^{1}H MRSI in the Human Prostate using a Double tuned Endorectal Coil at 7 tesla. *Magnetic Resonance in Medicine*, 72:1516-21.

Abstract

Purpose. Improved diagnostic sensitivity could be obtained in cancer detection and staging when individual compounds of the choline pool can be detected. Therefore a novel coil design is proposed, providing the ability to acquire both ^{1}H and ^{31}P MRSI in patients with prostate cancer.

Materials and Methods. A two-elements $^{1}H/^{31}P$ endorectal coil was designed by adjusting a commercially available 3T ERC. The 2-elements coil setup was interfaced as a transceiver to a whole body 7T MR-scanner. Simulations and phantom measurements were performed to compare the efficiency of the coil. ^{1}H MRSI and ^{31}P MRSI were acquired in vivo in prostate cancer patients.

Results. The efficiency of the $^{1}H/^{31}P$ coil is comparable to the dual channel ^{1}H coil previously published. Individually distinguishable phospholipid metabolites in the in vivo ^{31}P spectra were: PE, PC, Pi, GPE,GPC, PCr and ATP's. ^{1}H MRSI was performed within the same scan session, visualizing choline, polyamines, creatine and citrate.

Conclusions. ^{1}H MRSI and ^{31}P MRSI can be acquired in the human prostate at 7T within the same scan session, using an endorectal coil matched and tuned for ^{1}H (quadrature) and ^{31}P (linear) without the need of cable traps and with negligible efficiency losses in the ^{1}H and ^{31}P channel.

Introduction

A key problem of prostate cancer is patient selection for the appropriate treatment. Current staging is often inaccurate leading to overtreatment of low-risk or undertreatment of high-risk disease [11, 110].

Using MR spectroscopic imaging (MRSI), metabolites present in the human prostate can be detected and may be related to aggressiveness. The key metabolites observed in ^{1}H MR spectra of the prostate are total choline (tCho), polyamines (pa), creatine (cr) and citrate (cit). Changes in the choline metabolism are related to cancer malignancy [22, 23]. With ^{1}H MRSI the total choline and ethanolamine pool is measured, represented by tCho. The ratio between total choline and citrate has been correlated to the presence of cancer [24, 25]. However, accurate measurement of the tCho/cit ratio is challenging, as the tCho peak at 3.2 ppm in ^{1}H MRS is close to polyamines at 3.1 ppm and creatine at 3.0 ppm. Therefore the sum of all three metabolites is often considered instead of tCho only [26–28, 30].

With phosphorus (^{31}P) MRSI, four individual compounds within the ethanolamine and choline pool can be detected: phosphocholine (PC), glycerophosphocholine (GPC), phosphoethanolamine (PE) and glycerophosphoethanolamine (GPE). PC and PE are involved in membrane formation, GPC and GPE in membrane breakdown. In various tumor types a switch of high GPC and low PC in benign cells to high PC and low GPC in malignant cells has been observed [29, 30]. More recent, in vitro ^{31}P NMR measurements showed a significantly difference in PE and GPE (and their ratio) between cancer and benign prostatic hyperplasia [30]. Furthermore, ^{31}P NMR showed to be useful for discrimination between low-grade and high-grade cancer [30, 111]. This suggests that separating the tCho into its individual compounds may improve the accuracy of detecting and staging cancer.

As the sensitivity in detecting the metabolites with ^{31}P MRS is less than with ^{1}H MRS, ^{31}P MRS at a field strength of 1.5T or 3T is impaired by low signal-to-noise ratio (SNR) . However, using the SNR gain at 7T, the phospholipid metabolites can be detected in vivo using ^{31}P MRSI with a dedicated endorectal RF coil (ERC) [112]. In addition, the increased spectral resolution at higher magnetic field strength creates the possibility of individual detection of the metabolites, involving inorganic phosphate (Pi), phosphomonoesters (PME): PC and PE, phosphodiesters (PDE): GPC and GPE and the three ^{31}P signals of adenosine triphosphate (ATP).

So far, no reports have been published showing both ^{1}H and ^{31}P MRSI of the human prostate at 7T, acquired during the same scan session. First of all, for ^{1}H MRSI at 7T, an internal transmit coil is needed to provide the strong B_1^+ field required to minimize chemical shift displacement artifacts. Considering the asymmetric B_1^+ field distribution that a single coil provides at 7T, the combination with a stripline antenna has shown to provide a symmetric B_1^+ field and enabled accurate ^{1}H MRSI of the prostate at 7T using

the two channel ERC [44]. Secondly, a closely positioned surface loop coil is required to maximize the SNR of ^{31}P MRSI, which can be obtained with a ^{31}P ERC transceiver [112]. Consequently, an ERC is required as transceiver for both ^{1}H and ^{31}P. For the design of a double tuned coil it is crucial to maintain high sensitivity, both in transmit as receive, requiring lossless tank circuits. Fortunately, at 7T the tissue load is dominant, resulting in a negligible signal loss when using a tank circuit [113]. It is however critical to minimize the loading, and thus the contact with the surrounding tissue. This can be realized by using a small inductive loop for the tank circuit positioned at distance from conductive tissue.

In this study at 7T, we implemented a double tuned ERC as a two channel ^{1}H transceiver and a single channel ^{31}P transceiver using lossless tank circuits. Benefitting from high SNR and strong B_1 fields of the endorectal transceiver, broadband detection of the phospholipid metabolites was feasible while within the same scan session ^{1}H MRSI with minimal chemical shift dispersion could be obtained. Validated by phantom experiments, the detection of both ^{1}H and ^{31}P MR spectra in patients with prostate cancer using the ^{1}H/^{31}P ERC was demonstrated.

Methods

Hardware

A two-elements ^{1}H/^{31}P transmit and receive (TxRx) endorectal coil (ERC) was designed by modifying a commercially available 3T ERC (MEDRAD Inc., Indianola, PN) as described for ^{1}H by Arteaga *et al.* [44]. While the stripline is matched to 50 ohm at the ^{1}H frequency (298.2 MHz), the loop is matched to 50 ohm at both ^{1}H and ^{31}P (120.6 MHz) frequencies, Figure 5.1.

The capacitors in the single tuned ^{1}H loop were replaced by a tank circuit in series with another capacitor to enable tuning and matching on both frequencies, Figure 5.1A. This enables interfacing on a single port to enable connection with only a single coaxial cable for this double tuned coil, reducing the need of extra cables in the coil setup. The added losses of the tank circuit on both frequencies are minimized by keeping its field from the surrounding tissue, as low as possible [113]. The inductor of this tank circuit was designed as a solenoid with 3 turns and a 3.6-mm diameter, Figure 5.1B. The Q factor of the unloaded tank circuit was determined by $Q = f_{res}/\Delta f$ using two pickup probes for an S21 measurement with a network analyser (ZVL, Rohde&Schwarz). To prevent for cable coupling between the two coil elements, the grounds of the coaxial cables are connected at the entrance ports of the stripline and loop coil, avoiding the need for cable traps.

Simulations were performed to calculate the efficiency of the double-tuned ^{1}H/^{31}P endocoil versus a single tuned ^{1}H and ^{31}P coil using Cadence OrCad Capture (Berkshire,

United Kingdom) based on the circuit shown in Figure 5.1A.

The 2-element coil setup was interfaced to a whole body 7T MR-scanner (Philips Healthcare, Cleveland, OH) using a home-built interface box. By using two filters in parallel, one ^{1}H pass/^{31}P stop and the other ^{31}P pass/^{1}H stop, a circuit is created that splits the transmit/receive signal of the loop coil into a separate ^{1}H line and a ^{31}P line. The ^{1}H line continues to a quad hybrid in which the received signal is combined with the ^{1}H received signal of the stripline with a phase difference of 90°, while the transmit pulses are split to both ports with a -90° phase shift. The combined received ^{1}H signal is directed to a small band preamplifier, while transmit port is connected directly to the transmit amplifier. The ^{31}P line is connected to a small band transmit-receive switch and preamplifier.

The inner balloon of the ERC is filled with fluorinated fluid (Galden, Solvay Solexis, Milan, Italy) to match the susceptibility of the balloon with the prostate, hence minimizing B_0 shim artifacts.

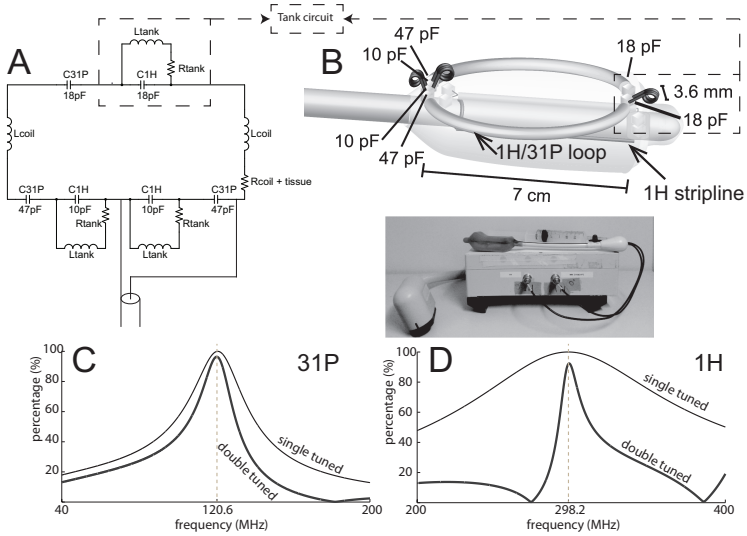

Figure 5.1: A) Schematics of the electronic circuit of the $^{1}H/^{31}P$ loop coil. B) Schematics of the ERC, containing both the $^{1}H/^{31}P$ loop and ^{1}H stripline. For a better view, the inductors of the tank circuits are displayed upwards, but in practice are pointing towards the guiding rod, in order to minimize tissue coupling. Below a photo of the setup including the interfacebox is shown. C/D) Results of the current density simulations for ^{1}H (298.2 MHz) and ^{31}P (120.6 MHz) normalized to their single tuned efficiencies. The double tuned loop has only a minor loss in current density compared to the single tuned loops (7,9 % for ^{1}H and 4,2 % for ^{31}P)

Patient	Age	PSA (ng/ml)	Gleason score
#1	66	8.6	3+3
#2	77	6.8	3+3
#3	60	11.4	3+3
#4	66	5.0	3+3
#5	69	6.2	3+3

Table 5.1: Patient characteristics.

Phantom measurements

A dual compartment phantom was used for the phantom measurements. One of the compartments was filled with denaturalized water and 6 g/L of NaCl to create the appropriate loading conditions for the ERC. The second compartment was filled with inorganic phosphate (Pi) that was used for a comparison between the double-tuned $^{1}H/^{31}P$ ERC and a single-tuned ^{31}P ERC. The ^{31}P MRSI grid was positioned covering the whole Pi filled compartment. To enable second order image based shimming a B_0 map (3D FFE, TE/TR=3.0/5.2 ms, acquisition matrix 64x84, 2.81x2.81x3mm^3 voxel, 20 slices) was acquired. To ensure relatively uniform signal detection over a 4 cm field of view a steady state ^{31}P MRSI sequence was used at a TR of 200 ms with Ernst angle excitation at the furthest distance of the coil (4 cm), and over-tipping close to the coil. For this, B_1 maps were estimated using multi angle 3D MRSI and a measured T1 of the phantom of 6 s. 3D MRSI was acquired using the following parameters (pulse acquire, TE/TR = 0.42/200 ms, 20x20x8 matrix, 12x12x12mm^3 voxel, acquisition time = 10.16 min). This sequence was repeated with the single-tuned ^{31}P ERC while using the same f_0 offset and shim parameters.

Patient measurements

Seven patients with biopsy-proven prostate cancer were scanned in supine position. Five patients were scanned with the novel $^{1}H/^{31}P$ ERC, Table 5.1. The two other patients (age: 63 and 61, PSA: 5.6 ng/ml and 13.4 ng/ml, both Gleason score: 6) were scanned with the quadrature ^{1}H ERC [44] for a comparison of the efficiency of the ERC. For this study written informed consent was obtained.

Gradient echo images (fast field echo (FFE), nominal flip angle = 45°, TR/TE = 23/2 ms, FOV = 500x500x3mm^3)were obtained for scouting. To show the appearance of transition bands formed when transmitting (Tx) with the ERC, extra gradient echo imaging was performed (FFE, TE/TR = 2.3/121 ms, 200x200 acquisition matrix, 2x2x3mm^3 voxel, 1 slice, nominal flip angle = 180°) in one patient with the double tuned setup and in two patients with the single tuned setup. This procedure enables to observe the Tx field strength with respect to the position of the ERC and assess efficiency of the ERC. T_2-weighted turbo spin echo (TSE) images were acquired for anatomy and tumor localization purposes

(TR/TE=5000/74 ms, 188x180 matrix, FOV = 150x150x58mmm^3, 10x 2mm^2 slices). A B_0 map (3D FFE, TE/TR = 3.0/5.2 ms, acquisition matrix 64x84, 2.81x2.81x3mm^3 voxel, 20 slices) was acquired to enable second order image based shimming.

The 2D ^{1}H MRSI grid was positioned in the tumor location as seen from the T_2-weighted images, while the 3D ^{31}P MRSI grid was positioned such to cover the whole prostate. ^{1}H 2D MRSI was acquired using the nsLASER [30,111], (TE/TR = 56/2000 ms, 24x8 matrix, acquired voxel size = 5x5x5mm^3, acquisition time = 7.46 min). ^{31}P 3D MRSI spectra were acquired using a steady state pulse acquire sequence, (TE/TR = 0.42/200 ms, nominal flip angle=20°, 20x20x8 matrix, acquired voxel size = 12x12x12mm^3, acquisition time = 10.16 min).

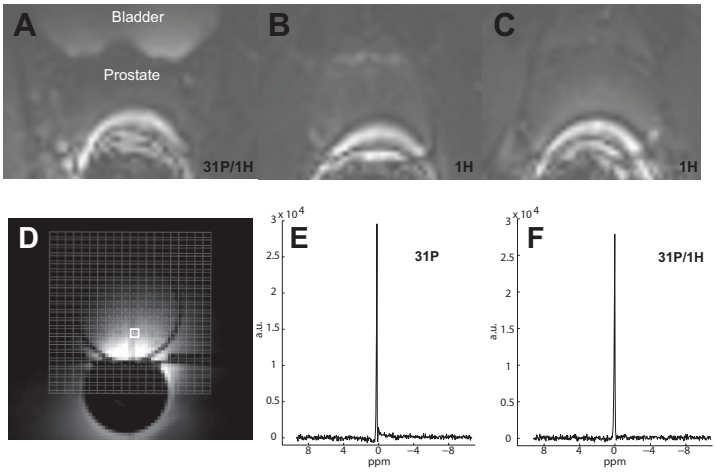

Figure 5.2: Efficiency of the $^{1}H/^{31}P$ ERC (A) is comparable to the dual channel ^{1}H ERC in 2 other patients (B,C), as shown by the similar pattern of transition bands in the gradient echo image. The SNR of the double tuned loop is close to 5 % less than that obtained with the single tuned ^{31}P loop using ^{31}P MRSI in a phantom (D/E/F).

Results

Q-factor measurements of the $^{1}H/^{31}P$ endorectal coil show that the effect of the tank circuit on the Q factor is very small, as the measured unloaded Q factor of the single tuned versus double tuned loop (Q = 243 and 213, respectively) was substantially higher than the loaded Q factor (Q = 8) for ^{1}H as for ^{31}P where the unloaded (Q = 248) versus loaded Q factor (Q = 24) differ by more than a factor of 10.

The simulations, Figure 5.1C, show that this relates to a loss of only 7.9% for ^{1}H and 4.2% for ^{31}P in B_1 efficiency when comparing the double tuned loop of the ERC with

single a tuned loop for each resonance (as determined by the current density in the loop coil per unit of delivered power).

Next to that, a transverse gradient echo image using a 180° nominal flip angle (Figure 5.2) shows that the efficiency of the $^{1}H/^{31}P$ coil is comparable to the dual channel ^{1}H ERC previously published [44]. The very high nominal excitation angle (180°) using a fixed RF power setting causes transition bands that are easily visible in the images. These accurately reflect the $B_1{}^{+}$ efficiency of the coil as only the areas where the actual flip angle matches the nominal flip angle (or multiplied by an integer) will cause signal voids. When comparing the acquired images with the double-tuned ERC to the proton only ERC, the distance of the transition bands to the ERC is not changed. A comparison of the SNR of 3D MRSI using the ^{31}P and the double-tuned $^{1}H/^{31}P$ ERC shows a close to 5% loss of signal, similar as that observed in the simulations (Figure 5.2D/E).

In all five patients the T_2-weighted images showed clear anatomical information of the apex, middle and base of the prostate. However the T_2-weighted TSE obtained with the ERC as a transceiver is very sensitive to the B_1field. In one patient B_0 shimming was not successful due to a defect in the ^{1}H part of the interface box, resulting in deteriorated ^{31}P MR spectra with broad linewidths and low signals in ^{1}H spectra.

The in vivo ^{1}H MR spectra obtained with the adiabatic nsLASER sequence (Figure 5.3A/B) show resolved resonances of choline (3.2 ppm), polyamines (3.1 ppm), creatine (3.0 ppm) and citrate (2.6 ppm). The signal of total choline does not overlap with the signal of polyamines. The total choline peak is increased in the tumor spectrum while the polyamines and citrate signals are decreased.

The in vivo ^{31}P MR spectra (Figure 5.3C/D) show resolved peaks of PE(6.7 ppm), PC (6.3 ppm), Pi (5.3 ppm), GPE (3.6 ppm),GPC (3.0 ppm, PCr (0 ppm), and ATPs (-2.6, -7.6 and -16.2 ppm) acquired in 10 minutes. Due to the short TR, optimal hamming weighted acquisition was applied providing minimal voxel bleeding of the surrounding muscle tissue (high PCr) while maintaining relatively high SNR, albeit potentially with a spatially dependent T1 contrast. Noticeable is that the Pi appears with 2 different peaks which might reflect Pi detection from compartments with different pH. When comparing the tumor and normal tissue in the prostate, the main differences are observed for the PME and PDE region as the PE signal decreases in the tumor location and thereby also the ratio of PE/PDE.

The sensitivity of the ERC is decreasing over distance, resulting in a limited coverage of the prostate where the SNR for PE or PC in ^{31}P MRS and for citrate or choline for ^{1}H MRS was higher than 3, Table 5.2.

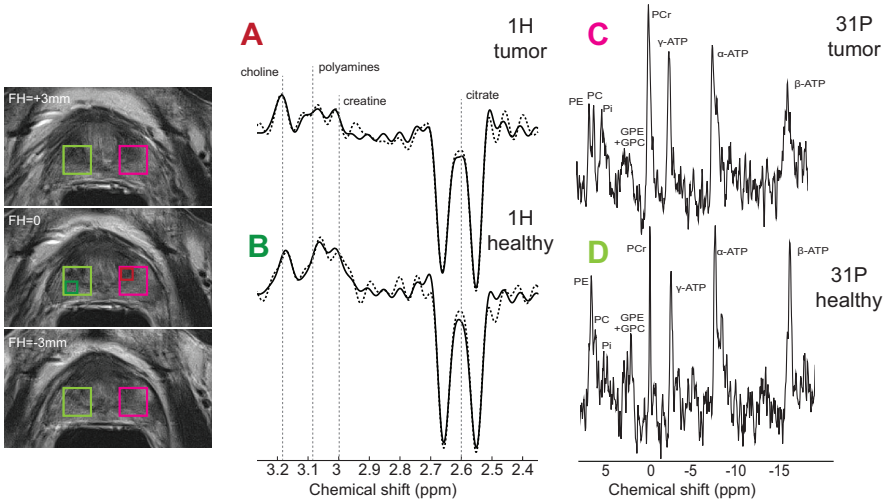

Figure 5.3: T_2-weighted image of the prostate indicating a healthy (green) and tumor (red) voxel. Please note that the ^{31}P voxel size is larger and therefore represented in 3 slices. A/B) ^{1}H MR spectrum of healthy and tumor area showing signals of total choline (Cho, 3.2 ppm), polyamines (PA, 3.1 ppm), creatine (Cre, 3.0 ppm) and citrate (Cit, 2.6 ppm). Noticeable is that the signal of total choline is increased and the polyamines signal reduced in the tumor area. The dashed line shows the original data, while the solid line represents the LCmodel fit. C) ^{31}P MR spectrum of tumor area. Notice the different signal intensitities of PE versus PC when comparing the spectrum obtained from tumor area to the spectrum obtained from healthy area. D) ^{31}P MR spectrum of healthy area, showing signals of PE (6.7 ppm), PC (6.3 ppm), Pi (5.3 and 5.1 ppm), GPE (3.6 ppm), GPC (3.0 ppm, PCr (0 ppm), ATP's (-2.6, -7.6 and -16.2 ppm).

Patient	^{31}P	^{1}H
#1	75 %	83 %
#2	60 %	66 %
#3	66 %	83 %
#4	25 %	-
#5	50 %	75 %

Table 5.2: Coverage of the prostate in anterior-posterior direction with a SNR > 3 for ^{1}H and ^{31}P MRS.

Discussion

In this work, we have shown that ^{1}H and ^{31}P MRSI could be combined in a single patient exam at a field strength of 7 T.

The addition of the tank circuit in the loop coil does not significantly influence the loaded Q factor and thereby the efficiency of the two-elements endorectal coil in comparison to a single tuned loop coil, similar as observed by Klomp et al. [113] for ^{13}C MRS in the human brain at 3T. Therefore, at 7T, the loop coil can be tuned to two frequencies without substantial penalties in sensitivity. Tissue loading of the stripline antenna is much less than the loading of a loop coil, hence only efficient at high frequencies [44]. Therefore, the stripline remained single tuned and matched to the high frequency of 298.2 MHz (^{1}H).

For ^{1}H MRSI distinct resonances of choline, polyamines, creatine and citrate could be detected, opening up the possibility for individual fitting, thereby increasing the sensitivity in detecting elevated choline levels from decreasing polyamine levels [28, 30, 97].

In this study, information of a two-dimensional slice was obtained using the nsLASER [98], thereby not covering the whole prostate. However, extension to 3D MRSI has shown to be feasible at 7T by incorporating reduced field of view encoding [98] or by applying echo planar readout trajectories [106]. So far we have used adiabatic RF pulses to obtain uniform excitation for ^{1}H MRS and positioned the slice through the tumor area.

The B_1 non-uniformities of the ERC are also reflected in the obtained T_2-weighted imaging of the prostate, resulting in impaired image quality due to transition bands. To compensate for the non-uniformities, adiabatic RF pulses could be used [114]. Another solution would be to use a combination of the proposed ^{1}H/^{31}P ERC together with ^{1}H external coils, as shown earlier for a ^{1}H ERC by Metzger et al. [45]. Kobus et al. [112] showed the combination of a ^{31}P ERC combined with ^{1}H external coils, with this setup optimal imaging can be acquired, however ^{1}H MRSI is impaired due to high SAR and chemical shift displacement artifacts.

The ^{31}P 3D MRSI in vivo measurements showed signals of phospholipid metabolites, comparable to results obtained with a single tuned ^{31}P ERC [112]. The following phospholipid metabolites could be detected, PE(6.7 ppm), PC (6.3 ppm), Pi (5.3 ppm), GPE (3.6 ppm), GPC (3.0 ppm, PCr (0 ppm), ATP's (-2.6, -7.6 and -16.2 ppm). Both PME and PDE resonances were detectable. In addition, PCr was observed that may originate from the surrounding muscle tissue, due to point spread and the relatively large voxel size in the ^{31}P measurements. It has been described that phosphoethanolamine (PE) is elevated and predominates in most human tumors [23, 30]. Our preliminary in vivo prostate results indicate the contrary, lower levels of phosphoethanolamine (PE) in the tumor areas compared to healthy tissue. This is in agreement with ex vivo prostate data published by Komoroski et al. [30].

Conclusion

In this study, we have shown that ^{1}H MRSI and ^{31}P MRSI can be acquired in the human prostate at 7T within the same scan session, using an endorectal coil matched and tuned for ^{1}H (quadrature) and ^{31}P (linear) without the need of cable traps and with negligible efficiency losses in the ^{1}H and ^{31}P channel. Obtaining both ^{1}H and ^{31}P MRSI using the newly designed $^{1}H/^{31}P$ ERC at 7T creates the possibility to study the choline metabolism in more detail. This could improve diagnostic sensitivity as the individual compounds of the choline pool may correlate better to tumor aggressiveness.

“Dans une grande âme,
tout est grand”

BLAISE PASCAL

6 General Discussion and Summary

6

Overdiagnosis and overtreatment of prostate cancer remain a major problem in patient care and may increase health costs. Non-invasive diagnostic imaging tools are of specific interest to assess prostate cancer aggressiveness and help the therapy decision-making process. Non-aggressive lesions may be followed up by a watch-full waiting program, including yearly examinations of the prostate, whereas potentially life threatening lesions deserve immediate measures. Therefore, it is necessary to have non-invasive tumor characterization methods for selective treatment of only those tumors which are potentially harmful.

Using anatomical T2- weighted imaging of the prostate at 3T a good distinction can be made between prostate cancer residing inside the prostate (T2-disease) and extracapsular disease (T3-disease) by experienced radiologists [115]. The progression of the tumors residing inside the prostate is hard to predict using the current imaging modalities. A recent systematic review by Fütterer et al. [116] concludes that due to the high negative predictive value multiparametric MRI (mpMRI) is useful to rule out significant disease. The accuracy, sensitivity and specificity ranges for detecting significant disease reported here were 44-87%, 58-96% and 23-87%, respectively. In spite improved diagnostic accuracy based on improved MRI and MRS based techniques, mpMRI still does not onbviate the need for ultrasound guides biopsies and prostatectomies remain of great importance to determine prostate cancer aggressiveness.

In this thesis, the use of ultra-high field MRI was investigated to improve noninvasive prostate cancer detection and aggressiveness characterization. The benefits of the higher SNR, spectral and spatial resolution at ultra-high field have been shown for T_2-weighted imaging, R2* mapping, ^{1}H and ^{31}P MRSI in the prostate. The prostate MR(S)I exams discussed in this thesis were all applied in patients with prostate cancer. However, clinical prostate examinations at 7T as a part of the routine clinical workflow are for numerous reasons still to be developed.

Imaging and SNR

In chapter 2, we have described an increase in intrinsic SNR of a factor of more than two at 7T, when compared to state-of-the-art 3T prostate imaging. Using this gain in SNR, high resolution T_2-weighted images were acquired of a prostate cancer patient using an external body array.

Imaging at 7T is technically challenging owing to RF inhomogeneities, increased tissue heating and reduced RF field penetration. Though numerous studies have documented the use of custom-built external arrays dedicated to prostate imaging at 7T to obtain adequate T_2-weighted imaging [45, 46, 48], the superior imaging performance of 7T over 3T was not demonstrated in terms of SNR [40]. Indeed, in vivo SNR comparisons between field strengths are challenging because of the wide range of different parameters used at

each field that make the comparison difficult. Relaxation time constants are different at different magnetic field strengths, thus requiring a different echo time and repetition time for optimum MRI at each field strength. Moreover, the RF coil arrays used are different; even if the identical coil geometry is used, a difference in the electromagnetic interaction with the body is expected at different fields, that is to say, an array optimized for one field will not be the optimal array for the other field. In addition, the uniformity of excitation also differs between field strengths, and leads to a spatial discrepancy between the nominal flip angle and that actually obtained in the patient. Finally, the upper SAR limit allowed during the imaging session may limit the use of optimized sequence parameters that may result in suboptimal scan efficiencies and SNR penalties.

The measured 2.1 fold gain in SNR as described in chapter 2 is not only beneficial for T_2-weighted imaging: MR spectroscopy, dynamic contrast enhanced sequences and diffusion weighted imaging are only a few of the prostate cancer characterization methods that can also profit from a higher SNR, while some of these MR techniques simultaneously also profit from an enhanced contrast mechanism at higher field strengths which comes on top of the SNR gain.

Endorectal coil

In chapter 3, 4 and 5 an endorectal coil (ERC) has been used, whereas only an external body array was applied at 7T in chapter 2. The use of an ERC is beneficial because of its location close to the prostate, resulting in a high local SNR and B_1 inside the prostate. Consequently, MRSI and R2* maps with a high spatial and spectral resolutions can be acquired. Another benefit of the ERC is the possibility to fill up the balloon with a tissue susceptibility matching fluid to minimize artifacts. Susceptibility effects, due to air-tissue interfaces for example, give rise to substantial artifacts at high field strengths. This is clearly visible in the prostate when the rectum is filled with gas naturally produced by the bowel. In R2* mapping the macroscopic susceptibility of the rectal gas pocket results in an artificial increase in R2* over the prostate that may be wrongly interpreted as a hypoxic area. In MRS this artifact causes broad line widths and disturbs individual metabolite detection.

The use of an ERC in clinical practice is a heavily discussed topic [117]. It depends on the protocols devised in each institution, and the preference of the radiologists. The practical use of ERCs in the daily practice implies the training of experienced technicians for the positioning of the ERC, along with the time it takes for the ERC insertion that must fit within the total scan time allocated per patient. Exam tolerability may be a limiting factor as some patients feel uncomfortable with the insertion of an ERC. Moreover, technical disadvantages include the B_1 inhomogeneity inherent to this surface coil, but also its low penetration depth. So far no traditional MRSI using only an external body

array was performed due to a lack of B_1 in the prostate; therefore, the use of ERCs at 7T is still relevant.

MRSI

^{1}H magnetic resonance spectroscopic imaging (MRSI) enables the detection of prostate metabolites including total choline (tCho), polyamines (PA, predominantly spermine), creatine (Cr) and citrate (Cit). These metabolites can be detected non-invasively (8,9). In vivo ^{1}H MRSI in the prostate has already proven to be useful for the detection of prostate cancer using the tCho/Cit ratio as choline levels increase and citrate levels decrease in aggressive prostate tumors [24, 35, 86, 88]. However, accurate measurement of the tCho/Cit ratio remains challenging, as the tCho peak is close to the PA and Cr resonances. Ex vivo studies show that tCho increases and PA as well as Cit decrease in prostate cancer tissue [90, 91, 105]. A significant decrease in the concentrations of polyamines and citrate has been shown when comparing high grade (Gleason score>7) to low grade (Gleason score<=6) tissue samples [91].

In chapter 4, the separate detection of total choline from the polyamines was demonstrated at 7T, opening up the possibility to acquire the more specific ratio of tCho /Cit instead of the commonly used ratio ((Cho+PA+Cr)/Cit) at lower field strengths. The high-quality spectra acquired in this study could possibly be optimized even further by using field probes to get more insight into the B_0 fluctuations in the prostate, due to e.g. bowel movements, and the possibility to correct for these [118]. Furthermore, MRSI data in only one slice of the prostate was obtained, while in studies at 1.5 and 3T the whole prostate area is covered using 3D ^{1}H MRSI [24, 35]. Extension to 3D MRSI may be feasible at 7T by incorporating reduced field of view encoding [42] or by applying echo planar readout trajectories [106].

In chapter 5, phosphorus (^{31}P) MRSI was successfully added to the scan protocol by using a dedicated double tuned ERC. With ^{31}P MRSI, four individual compounds within the choline and ethanolamine pool can be detected: phosphocholine (PC), glycerophosphocholine (GPC), phosphoethanolamine (PE) and glycerophosphoethanolamine (GPE). PC and PE are involved in membrane formation, GPC and GPE in membrane breakdown. As the sensitivity in detecting the metabolites with ^{31}P MRS is less than that with ^{1}H MRS, ^{31}P MRS at a field strength of 1.5T or 3T is impaired by low signal-to-noise ratio (SNR). However, using the SNR gain offered at 7T MRI, the phospholipid metabolites can be detected in vivo. It has been described that phosphoethanolamine (PE) is elevated and is predominant in most human tumors [23]. On the contrary, our preliminary in vivo prostate results indicate lower levels of phosphoethanolamine (PE) in tumor areas compared to healthy tissue. This observation is in agreement with ex vivo prostate data published by Komoroski et al. [30]. In other in vivo studies at 7T, no differences

in metabolite ratios were reported [41]. Large voxels are commonly used for ^{31}P MRSI because of the low concentration of ^{31}P metabolites, thus reducing the possibility to collect the metabolite content from small prostate tumors. Hence there is a clear relevance to devise new methodologies in order to increase the spatial resolution and the acquisition time. Nowadays, research is performed to increase the SNR of ^{31}P MRSI by e.g. polarization transfer, NOE effect and multi echo methods [119–121].

Scan time; SAR limitations and preparation time

Although penetration of the RF signals is limited at 7T, deep anatomical structures, such as the prostate, can be imaged at this high field strength due to constructive interferences of multiple RF waves emitted via antennas. While some inhomogeneity of the RF magnetic field remains, the heating caused by the RF electric field in the body is the major challenge at 7T. Power deposition in the body can be evaluated by means of the specific absorption rates (SAR). As SAR measurement is practically impossible in vivo, simulations are widely used to amount of heating inside the body.

In chapter 2, 4 and 5, we obtained the T_2-weighted images and ^{1}H spectroscopy with only one slice to avoid local SAR violations. Currently, tools and adapted sequences are being designed and developed to reduce the uncertainties in SAR levels between subjects and provide more accurate SAR assessments without the overestimations used in this thesis [46, 56]. Moreover, RF pulse trains are being designed that more evenly distributes heat to substantially reduce the (local) SAR.

In our studies, we had to increase scan time by approximately 3 minutes which was needed to acquire the individual transmit element field patterns and optimize the phase settings for constructive interference of the B_1 fields in the prostate when using the external body array (B_1 shimming). In addition, time was needed for B_0 shimming, assuring small linewidths in spectroscopy.

In the future it is expected that all these time limiting factors may be reduced by newly developed software, sequences and self-adjusting settings for all patients.

Conclusion

Although the potential benefit of prostate examinations at 7 T including R2* mapping, ^{31}P and ^{1}H MRSI needs to be shown in clinical trials, our studies have exposed much more characteristics of prostate tissue in vivo. Using R2* mapping, chapter 3, it was shown that by diminishing potential artifacts and by higher spatial resolutions at 7T the measured R2* was closer to the intrinsic R2* than measured at 3T. The benefits of the higher spectral resolution were of importance while acquiring ^{1}H MRSI of prostate cancer patients, here the separate detection of total choline and polyamines opened up

the possibility for calculating the tCho/Cit ratio. Furthermore, the short echo time used at 7T revealed a total of 7 distinctive metabolites that could be detected and quantified in prostate tissue in vivo. In chapter 5, the combination of ^{1}H and ^{31}P MRSI in a single patient exam was shown for the first time. Lower levels of phosphoethanolamine (PE) in tumor areas compared to healthy tissue were detected, which particularly when combined with all of the newly obtained parameters might potentially give more information on tumor aggressiveness.

Future directions

As shown in this thesis prostate MR(S)I is possible with high spectral and spatial resolutions at 7T. Further research to bring 7T prostate imaging to the clinic should be conducted.

First, scan time reduction is needed for all the methods described in this thesis, as a single patient examination should be fitted in a window of 45 minutes. Speed-up techniques such as EPI readouts would be beneficial for MRSI. In addition, preparation times for e.g. B_1 shimming could be reduced by automatic processes. More importantly, larger prospective patient studies with a broader range of Gleason scores are necessary to visualize the potential benefits in detecting prostate cancer aggressiveness in vivo using the new parameters that ultra-high field strength MR(S)I can bring. In the near future, the 7T META-scanner will be installed in the UMC Utrecht, opening up the possibility to acquire data in patients for 5 different nuclei. Other nuclei than discussed here might give additional information about the tumor metabolism, for example using by ^{23}Na, that could lead to a better insight into necrotic vs malignant tissue.

Summary

Nowadays, MRI is increasingly used in clinical practice to detect the primary prostate tumor. However, despite the use of higher magnetic field strengths (up to 3T), the characterization of tumor aggressiveness remains limited. In this thesis, new methodologies using ultra-high field MRI (7T) have been developed and evaluated for the non-invasive assessment of prostate cancer aggressiveness.

The first study (chapter 2) shows a new coil configuration with both antennas and loops in a surface coil array for prostate imaging at 7 tesla. Using this setup, we demonstrated for the first time the gain in SNR and resolution that can be achieved with the higher field strength of 7 tesla for prostate MR imaging using only external elements. Compared to a clinically used prostate imaging setup at 3 tesla, 7 tesla imaging resulted in an overall gain in SNR of 2.1-fold. Furthermore, high resolution imaging was obtained at 7 tesla in one prostate cancer patient, to show the potential of going up to ultra-high field prostate imaging with ultra-high resolutions.

Chapter 3 describes the usage of R2* imaging of the prostate at both 3 and 7 tesla. R2* imaging has been reported to be a promising tool for hypoxia imaging, particularly when minimizing macroscopic susceptibility effects such as the presence of rectal gas. In 85% of the patients without gas pockets the tumor suspected region was significantly different in R2* values compared to the surrounding healthy tissue. Yet, even in this group, macroscopic effects are still substantial, as demonstrated in comparison to ultra-high resolution R2* mapping at 7 tesla.

In chapter 4, the potential benefits for ^{1}H MRSI in the prostate at ultra-high field are investigated. In contrast to MRSI at lower field strengths, where polyamine signals overlap with choline signals, our results at 7T demonstrate the ability to detect seven metabolites distinctively. This facilitated the investigation of the role of multiple metabolites in prostate cancer when acquired with ^{1}H MRSI. When based on traditional imaging features to identify the tumor, only the conventional metabolite ratio (tCho+PA+Cr)/Cit significantly discriminates between low grade tumor and healthy tissue at 7 tesla. Any combination of the seven metabolites had none or a less discriminating power at inter-patient level when compared to the traditional ratio.

Finally in chapter 5, we have shown that ^{1}H MRSI and ^{31}P MRSI can be acquired in the human prostate at 7T within the same scan session, using an endorectal coil matched and tuned for ^{1}H (quadrature) and ^{31}P (linear) without the need of cable traps and with negligible efficiency losses in the ^{1}H and ^{31}P channel. Obtaining both ^{1}H and ^{31}P MRSI using the newly designed ^{1}H/ ^{31}P ERC at 7 tesla creates the possibility to study the choline metabolism in more detail. This could improve diagnostic sensitivity as the individual compounds of the choline pool may correlate better to tumor aggressiveness.

Nederlandse samenvatting

Tegenwoordig wordt er voor de diagnostiek van prostaatkanker meer en meer gebruik gemaakt van de MRI. Tot op heden kan, ondanks de hogere veldsterktes van de huidige MRI's, de agressiviteit van de tumor nog niet goed in kaart worden gebracht. In dit proefschrift zijn nieuwe methodes ontwikkeld en getest om de agressiviteit van prostaattumoren in beeld te brengen.

In de eerste studie (hoofdstuk 2) wordt een nieuwe meetopstelling onderzocht welke wordt gebruikt voor beeldvorming van de prostaat op 7 tesla MRI. Met deze opstelling wordt voor de eerste keer de voordelen van de externe antennes (spoelen) voor prostaat beeldvorming aangetoond. Zo is er ten opzichte van de lagere veldsterkte van 3 tesla een verdubbeling van de signaal-ruis-ratio gemeten. Daardoor konden er anatomische beelden van de prostaat met hoge resolutie verkregen worden van een patiënt met prostaatkanker.

Hoofdstuk 3 beschrijft het gebruik van R2* beeldvorming van de prostaat op zowel 3 als 7 tesla. R2* kan mogelijk gebruikt worden om de zuurstofspanning in de tumor te meten, echter kunnen er artefacten ontstaan door gas wat in het rectum aanwezig kan zijn. In deze patiëntenstudie werd in 85% van de patiënten zonder gas in het rectum een verschil gevonden in R2* waarden tussen de tumor en het omliggende gezonde weefsel. Echter waren ook in deze groep op 3 tesla nog steeds macroscopische susceptibiliteit effecten gezien, welke verminderen op 7 tesla door het gebruik van een hogere resolutie meetmethode.

In hoofdstuk 4 en 5 wordt met behulp van de toename in signaal-ruis-ratio de agressiviteit van prostaattumoren in kaart gebracht door middel van het gebruik van 1H en 31P magnetische resonantie spectroscopie (MRS). Hiermee kan naar de celdeling en het energie metabolisme van de tumor en het omringende gezonde weefsel gekeken worden zonder het daadwerkelijke invasief weefsel te verkrijgen middels operatie of biopsie. Door de korte echo tijd die wordt gebruikt op 7 tesla kunnen in vivo in de prostaat 7 verschillende metabolieten gemeten worden.

De ontwikkelde en geteste methodes beschreven in dit proefschrift gebruik makend van een 7 tesla MRI laten allen een toegevoegde waarde zien in beeldvorming van prostaat kanker, welke ingezet kunnen worden in klinische studies naar validatie van beeldvorming van agressiviteit.

7 References

[1] J. Ferlay, I. Soerjomataram, R. Dikshit, S. Eser, C. Mathers, M. Rebelo, D. M. Parkin, D. Forman, and F. Bray, "Cancer incidence and mortality worldwide: sources, methods and major patterns in GLOBOCAN 2012," *Int. J. Cancer*, vol. 136, no. 5, pp. E359–E386, 2015.

[2] R. L. Siegel, K. D. Miller, and A. Jemal, "Cancer statistics, 2015," *CA. Cancer J. Clin.*, vol. 65, no. 1, pp. 5–29, 2015.

[3] G. Draisma, R. Boer, S. J. Otto, I. W. van der Cruijsen, R. A. Damhuis, F. H. Schröder, and H. J. de Koning, "Lead times and overdetection due to prostate-specific antigen screening: estimates from the European Randomized Study of Screening for Prostate Cancer," *J. Natl. Cancer Inst.*, vol. 95, no. 12, pp. 868–878, 2003.

[4] S. Loeb, M. A. Bjurlin, J. Nicholson, T. L. Tammela, D. F. Penson, H. B. Carter, P. Carroll, and R. Etzioni, "Overdiagnosis and Overtreatment of Prostate Cancer," *Eur. Urol.*, vol. 65, pp. 1046–1055, June 2014.

[5] C. Magi-Galluzzi and C. G. Przybycin, eds., *Genitourinary Pathology*. New York, NY: Springer New York, 2015.

[6] D. F. Gleason, "Histologic grading of prostate cancer: a perspective," *Hum. Pathol.*, vol. 23, no. 3, pp. 273–279, 1992.

[7] K. Mistry and G. Cable, "Meta-analysis of prostate-specific antigen and digital rectal examination as screening tests for prostate carcinoma," *J. Am. Board Fam. Pract.*, vol. 16, no. 2, pp. 95–101, 2003.

[8] S. Fine and J. Epstein, "A contemporary study correlating prostate needle biopsy and radical prostatectomy Gleason score," *J. Urology*, 2008.

[9] M. S. Cookson, N. E. Fleshner, S. M. Soloway, and W. R. Fair, "Correlation between Gleason score of needle biopsy and radical prostatectomy specimen: accuracy and clinical implications," *J. Urology*, vol. 157, no. 2, pp. 559–562, 1997.

[10] H. Hricak, R. Williams, D. Spring, K. Moon Jr, M. Hedgcock, R. Watson, and L. Crooks, "Anatomy and pathology of the male pelvis by magnetic resonance imaging," *Am. J. Roentgenol.*, vol. 141, no. 6, pp. 1101–1110, 1983.

[11] J. O. Barentsz, J. Richenberg, R. Clements, P. Choyke, S. Verma, G. Villeirs, O. Rouviere, V. Logager, and J. J. Futterer, "ESUR prostate MR guidelines 2012," *Eur. Radiol.*, vol. 22, no. 4, pp. 746–57, 2012.

[12] J. O. Barentsz, J. C. Weinreb, S. Verma, H. C. Thoeny, C. M. Tempany, F. Shtern, A. R. Padhani, D. Margolis, K. J. Macura, M. A. Haider, F. Cornud, and P. L. Choyke, "Synopsis of the PI-RADS v2 Guidelines for Multiparametric Prostate Magnetic Resonance Imaging and Recommendations for Use," *Eur. Urol.*, vol. 69, pp. 41–49, Jan. 2016.

[13] R. Nagarajan, D. Margolis, S. Raman, M. K. Sarma, K. Sheng, C. R. King, G. Verma, J. Sayre, R. E. Reiter, and M. A. Thomas, "MR spectroscopic imaging and diffusion-weighted imaging of prostate cancer with Gleason scores.," *J. Magn. Res. Im.*, vol. 36, pp. 697–703, 2012.

[14] S. Verma and A. Rajesh, "A clinically relevant approach to imaging prostate cancer: review.," *Am. J. Roentgenology*, vol. 196, pp. S11–4, 2011.

[15] Y. Itou, K. Nakanishi, Y. Narumi, Y. Nishizawa, and H. Tsukuma, "Clinical utility of apparent diffusion coefficient (ADC) values in patients with prostate cancer: can ADC values contribute to assess the aggressiveness of prostate cancer?," *J. Magn. Res. Im.*, vol. 33, pp. 167–72, 2011.

[16] C. Testa, R. Schiavina, R. Lodi, E. Salizzoni, B. Corti, M. Farsad, J. Kurhanewicz, F. Manferrari, E. Brunocilla, C. Tonon, and others, "Prostate Cancer: Sextant Localization with MR Imaging, MR Spectroscopy, and 11c-Choline PET/CT 1," *Radiology*, vol. 244, no. 3, pp. 797–806, 2007.

[17] P. S. Tofts, G. Brix, D. L. Buckley, J. L. Evelhoch, E. Henderson, M. V. Knopp, H. B. Larsson, T.-Y. Lee, N. A. Mayr, and G. J. Parker, "Estimating kinetic parameters from dynamic contrast-enhanced T 1-weighted MRI of a diffusable tracer: standardized quantities and symbols," *J. Magn. Reson. Imaging*, vol. 10, no. 3, pp. 223–232, 1999.

[18] A. Turaka, M. K. Buyyounouski, A. L. Hanlon, E. M. Horwitz, R. E. Greenberg, and B. Movsas, "Hypoxic prostate/muscle PO2 ratio predicts for outcome in patients with localized prostate cancer: long-term results.," *Int. J. Radiat. Oncol. Biol. Phys.*, vol. 82, pp. e433–9, 2012.

[19] R. Vergis, C. M. Corbishley, A. R. Norman, J. Bartlett, S. Jhavar, M. Borre, S. Heeboll, A. Horwich, R. Huddart, V. Khoo, R. Eeles, C. Cooper, M. Sydes, D. Dearnaley, and C. Parker, "Intrinsic markers of tumour hypoxia and angiogenesis in localised prostate cancer and outcome of radical treatment: a retrospective analysis of two randomised radiotherapy trials and one surgical cohort study.," *Lancet Oncol.*, vol. 9, pp. 342–51, 2008.

[20] S. Chopra, W. D. Foltz, M. F. Milosevic, A. Toi, R. G. Bristow, C. Ménard, and M. a. Haider, "Comparing oxygen-sensitive MRI (BOLD R2*) with oxygen electrode measurements: a pilot study in men with prostate cancer.," *Int. J. Radiat. Biol.*, vol. 85, pp. 805–13, 2009.

[21] P. J. Hoskin, D. M. Carnell, N. J. Taylor, R. E. Smith, J. J. Stirling, F. M. Daley, M. I. Saunders, S. M. Bentzen, D. J. Collins, J. a. d'Arcy, and A. P. Padhani, "Hypoxia in prostate cancer: correlation of BOLD-MRI with pimonidazole immunohistochemistry-initial observations.," *Int. J. Radiat. Oncol. Biol. Phys.*, vol. 68, pp. 1065–71, 2007.

[22] E. Aboagye and Z. Bhujwalla, "Malignant transformation alters membrane choline phospholipid metabolism of human mammary epithelial cells," *Cancer Res.*, 1999.

[23] F. Podo, "Tumour phospholipid metabolism.," *NMR Biomed.*, vol. 12, pp. 413–39, 1999.

[24] J. Kurhanewicz, D. B. Vigneron, H. Hricak, P. Narayan, P. Carroll, and S. J. Nelson, "Three-dimensional H-1 MR spectroscopic imaging of the in situ human prostate with high (0.24-0.1-cm(3)) spatial resolution," *Radiology*, vol. 198, no. 3, pp. 795–805, 1996.

[25] A. P. Chen, C. H. Cunningham, J. Kurhanewicz, D. A. Xu, R. E. Hurd, J. M. Pauly, L. Carvajal, K. Karpodinis, and D. B. Vigneron, "High-resolution 3d MR spectroscopic imaging of the prostate at 3 T with the MLEV-PRESS sequence," *Magn. Reson. Imaging*, vol. 24, no. 7, pp. 825–832, 2006.

[26] G. M. Villeirs, G. O. De Meerleer, P. J. De Visschere, V. H. Fonteyne, A. C. Verbaeys, and W. Oosterlinck, "Combined magnetic resonance imaging and spectroscopy in the assessment of high grade prostate carcinoma in patients with elevated psa: a single-institution experience of 356 patients," *Eur. J. Radiol.*, vol. 77, no. 2, pp. 340–345, 2011.

[27] T. W. J. Scheenen, J. Fütterer, E. Weiland, P. van Hecke, M. Lemort, C. Zechmann, H.-P. Schlemmer, D. Broome, G. Villeirs, J. Lu, J. Barentsz, S. Roell, and A. Heerschap, "Discriminating cancer from noncancer tissue in the prostate by 3-dimensional proton magnetic resonance spectroscopic imaging: a prospective multicenter validation study.," *Invest. Radiol.*, vol. 46, pp. 25–33, 2011.

[28] A. Shukla-Dave, H. Hricak, C. Moskowitz, N. Ishill, O. Akin, K. Kuroiwa, J. Spector, M. Kumar, V. E. Reuter, J. A. Koutcher, and K. L. Zakian, "Detection of Prostate Cancer with MR Spectroscopic Imaging: An Expanded Paradigm Incorporating Polyamines," *Radiology*, vol. 245, pp. 499–506, 2007.

[29] K. Glunde and Z. Bhujwalla, "Metabolic tumor imaging using magnetic resonance spectroscopy," *Semin. Oncol.*, 2011.

[30] R. A. Komoroski, J. C. Holder, A. A. Pappas, and A. E. Finkbeiner, "31p nmr of phospholipid metabolites in prostate cancer and benign prostatic hyperplasia," *Magn. Reson. Med.*, vol. 65, no. 4, pp. 911–913, 2011.

[31] A. Shukla-Dave and H. Hricak, "Role of mri in prostate cancer detection," *NMR Biomed.*, vol. 27, no. 1, pp. 16–24, 2014.

[32] C. Tempany and F. Franco, "Prostate mri: Update and current roles," *Appl. Radiol.*, vol. 41, no. 3, p. 17, 2012.

[33] T. W. Scheenen, A. B. Rosenkrantz, M. A. Haider, and J. J. Fütterer, "Multiparametric magnetic resonance imaging in prostate cancer management: current status and future perspectives," *Invest. Radiol.*, vol. 50, no. 9, pp. 594–600, 2015.

[34] B. Turkbey, A. M. Brown, S. Sankineni, B. J. Wood, P. A. Pinto, and P. L. Choyke, "Multiparametric prostate magnetic resonance imaging in the evaluation of prostate cancer: MRI of Prostate Cancer," *CA. Cancer J. Clin.*, vol. 66, pp. 326–336, July 2016.

[35] T. Kobus, T. Hambrock, C. a. Hulsbergen-van de Kaa, A. J. Wright, J. O. Barentsz, A. Heerschap, and T. W. J. Scheenen, "In vivo assessment of prostate cancer aggressiveness using magnetic resonance spectroscopic imaging at 3 T with an endorectal coil.," *Eur. Urol.*, vol. 60, pp. 1074–80, 2011.

[36] J. Kurth, E. Defeo, and L. L. Cheng, "Magnetic resonance spectroscopy: a promising tool for the diagnostics of human prostate cancer?," *Urol. Oncol.*, vol. 29, pp. 562–71, 2011.

[37] E. K. Vos, T. Kobus, G. J. Litjens, T. Hambrock, C. A. Hulsbergen-van de Kaa, J. O. Barentsz, M. C. Maas, and T. W. Scheenen, "Multiparametric Magnetic Resonance Imaging for Discriminating Low-Grade From High-Grade Prostate Cancer," *Invest. Radiol.*, vol. 50, no. 8, pp. 490–497, 2015.

[38] J. J. Fütterer, T. W. Scheenen, H. J. Huisman, D. W. Klomp, F. A. van Dorsten, C. A. Hulsbergen–van de Kaa, J. A. Witjes, A. Heerschap, and J. O. Barentsz, "Initial experience of 3 tesla endorectal coil magnetic resonance imaging and 1h-spectroscopic imaging of the prostate," *Invest. Radiol.*, vol. 39, no. 11, pp. 671–680, 2004.

[39] D. M. Cornfeld and J. C. Weinreb, "MR imaging of the prostate: 1.5 T versus 3t," *Magn. Reson. Imaging Clin. N. Am.*, vol. 15, no. 3, pp. 433–448, 2007.

[40] E. Vos, M. Lagemaat, J. Barentsz, J. Fütterer, P. Zámecnik, H. Roozen, S. Orzada, A. Bitz, M. Maas, and T. Scheenen, "Image quality and cancer visibility of T2-weighted Magnetic Resonance Imaging of the prostate at 7 Tesla," *Eur. Radiol.*, vol. 24, no. 8, pp. 1950–1958, 2014.

[41] M. W. Lagemaat, E. K. Vos, M. C. Maas, A. K. Bitz, S. Orzada, M. J. van Uden, T. Kobus, A. Heerschap, and T. W. Scheenen, "Phosphorus magnetic resonance spectroscopic imaging at 7 T in patients with prostate cancer," *Invest. Radiol.*, vol. 49, no. 5, pp. 363–372, 2014.

[42] M. W. Lagemaat, V. Breukels, E. K. Vos, A. B. Kerr, M. J. van Uden, S. Orzada, A. K. Bitz, M. C. Maas, and T. W. Scheenen, "1h MR spectroscopic imaging of the prostate at 7t using spectral-spatial pulses," *Magn. Reson. Med.*, 2015.

[43] M. P. Luttje, M. G. Italiaander, C. S. Arteaga de Castro, W. J. Kemp, P. R. Luijten, M. Vulpen, U. A. Heide, and D. W. Klomp, "31p MR spectroscopic imaging combined with 1h MR spectroscopic imaging in the human prostate using a double tuned endorectal coil at 7t," *Magn. Reson. Med.*, vol. 72, no. 6, pp. 1516–1521, 2014.

[44] C. S. Arteaga de Castro, B. van den Bergen, P. R. Luijten, U. a. van der Heide, M. van Vulpen, and D. W. J. Klomp, "Improving SNR and B1 transmit field for an endorectal coil in 7 T MRI and MRS of prostate cancer.," *Magn. Reson. Med.*, vol. 68, pp. 311–8, 2012.

[45] G. J. Metzger, P. F. van de Moortele, C. Akgun, C. J. Snyder, S. Moeller, J. Strupp, P. Andersen, D. Shrivastava, T. Vaughan, K. Ugurbil, and G. Adriany, "Performance of External and Internal Coil Configurations for Prostate Investigations at 7 T," *Magn. Reson. Med.*, vol. 64, no. 6, pp. 1625–1639, 2010.

[46] M. C. Maas, E. K. Vos, M. W. Lagemaat, A. K. Bitz, S. Orzada, T. Kobus, O. Kraff, S. Maderwald, M. E. Ladd, and T. W. Scheenen, "Feasibility of T2-weighted turbo spin echo imaging of the human prostate at 7 tesla," *Magn. Reson. Med.*, vol. 71, no. 5, pp. 1711–1719, 2014.

[47] A. Raaijmakers, O. Ipek, D. Klomp, C. Possanzini, P. Harvey, J. Lagendijk, and C. Van den Berg, "Design of a radiative surface coil array element at 7 T: The single-side adapted dipole antenna," *Magn. Reson. Med.*, vol. 66, no. 5, pp. 1488–1497, 2011.

[48] A. J. Raaijmakers, M. Italiaander, I. J. Voogt, P. R. Luijten, J. M. Hoogduin, D. W. Klomp, and C. A. van den Berg, "The fractionated dipole antenna: A new antenna for body imaging at 7 Tesla," *Magn. Reson. Med.*, vol. 75, pp. 1366–1374, 2015.

[49] A. B. Rosenkrantz, B. Zhang, N. Ben-Eliezer, J. Nobin, J. Melamed, F. Deng, S. S. Taneja, and G. C. Wiggins, "T2-weighted prostate MRI at 7 tesla using a simplified external transmit-receive coil array: Correlation with radical prostatectomy findings in two prostate cancer patients," *J. Magn. Reson. Imaging*, vol. 41, no. 1, pp. 226–232, 2015.

[50] P. B. Roemer, W. A. Edelstein, C. E. Hayes, S. P. Souza, and O. Mueller, "The NMR phased array," *Magn. Reson. Med.*, vol. 16, no. 2, pp. 192–225, 1990.

[51] V. L. Yarnykh, "Actual flip-angle imaging in the pulsed steady state: a method for rapid three-dimensional mapping of the transmitted radiofrequency field," *Magn. Reson. Med.*, vol. 57, no. 1, pp. 192–200, 2007.

[52] J. Sosna, I. Pedrosa, W. C. Dewolf, H. Mahallati, R. E. Lenkinski, and N. M. Rofsky, "MR imaging of the prostate at 3 Tesla: comparison of an external phased-array coil to imaging with an endorectal coil at 1.5 Tesla," *Acad. Radiol.*, vol. 11, no. 8, pp. 857–862, 2004.

[53] Y. Mazaheri, A. Shukla-Dave, A. Muellner, and H. Hricak, "MRI of the prostate: clinical relevance and emerging applications.," *J. Magn. Reson. Im.*, vol. 33, pp. 258–74, 2011.

[54] A. Raaijmakers, O. Ipek, W. Koning, H. Kroeze, C. Possanzini, P. Harvey, D. W. Klomp, P. Luijten, J. J. Lagendijk, and C. Van den Berg, "Highly accelerated 7 T prostate imaging using parallel imaging," *Proceedings ISMRM 2011, Montreal, Canada*, p. 166, 2011.

[55] F. Wiesinger, V. de Moortele, G. Adriany, N. De Zanche, K. Ugurbil, and K. P. Pruessmann, "Potential and feasibility of parallel MRI at high field," *NMR Biomed.*, vol. 19, no. 3, pp. 368–378, 2006.

[56] A. Sbrizzi, H. Hoogduin, J. J. Lagendijk, P. Luijten, G. L. Sleijpen, and C. A. van den Berg, "Fast design of local N-gram-specific absorption rate–optimized radiofrequency pulses for parallel transmit systems," *Magn. Reson. Med.*, vol. 67, no. 3, pp. 824–834, 2012.

[57] R. Alonzi, N. J. Taylor, J. J. Stirling, J. a. d'Arcy, D. J. Collins, M. I. Saunders, P. J. Hoskin, and A. R. Padhani, "Reproducibility and correlation between quantitative and semiquantitative dynamic and intrinsic susceptibility-weighted MRI parameters in the benign and malignant human prostate.," *J. Magn. Reson. Imaging*, vol. 32, pp. 155–64, 2010.

[58] L. Jiang, D. Zhao, A. Constantinescu, and R. P. Mason, "Comparison of BOLD contrast and Gd-DTPA dynamic contrast-enhanced imaging in rat prostate tumor.," *Magn. Reson. Med.*, vol. 51, pp. 953–60, 2004.

[59] R. Alonzi, A. R. Padhani, N. J. Taylor, D. J. Collins, J. a. D'Arcy, J. J. Stirling, M. I. Saunders, and P. J. Hoskin, "Antivascular effects of neoadjuvant androgen deprivation for prostate cancer: an in vivo human study using susceptibility and relaxivity dynamic MRI.," *Int. J. Radiat. Oncol. Biol. Phys.*, vol. 80, pp. 721–7, 2011.

[60] A. Dal Pra, M. Milosevic, R. Hill, B. Wouters, P. Warde, and R. G. Bristow, "Hypoxia, Androgen Deprivation and Systemic Metastases in Prostate Cancer (In Response to "Antivascular Effects of Neoadjuvant Androgen Deprivation for Prostate Cancer: An In Vivo Human Study Using Susceptibility and Relaxitivity Dynamic MRI": In Regard to," *Int. J. Radiat. Oncol. Biol. Phys.*, vol. 82, p. 1319, 2012.

[61] K. R. Thulborn, S. Y. Chang, G. X. Shen, and J. T. Voyvodic, "High-resolution echo-planar fMRI of human visual cortex at 3.0 tesla," *NMR Biomed.*, vol. 10, no. 4-5, pp. 183–190, 1997.

[62] J. R. Reichenbach, R. Venkatesan, D. A. Yablonskiy, M. R. Thompson, S. Lai, and E. M. Haacke, "Theory and application of static field inhomogeneity effects in gradient-echo imaging," *J. Magn. Reson. Imaging*, vol. 7, no. 2, pp. 266–79, 1997.

[63] A. M. Peters, M. J. Brookes, F. G. Hoogenraad, P. a. Gowland, S. T. Francis, P. G. Morris, and R. Bowtell, "T2* measurements in human brain at 1.5, 3 and 7 T.," *Magn. Reson. Imaging*, vol. 25, pp. 748–53, 2007.

[64] H. Choi and J. Ma, "Use of perfluorocarbon compound in the endorectal coil to improve MR spectroscopy of the prostate.," *AJR Am. J. Roentgenol.*, vol. 190, pp. 1055–9, 2008.

[65] Y. Rosen, B. N. Bloch, R. E. Lenkinski, R. L. Greenman, R. P. Marquis, and N. M. Rofsky, "3t MR of the prostate: reducing susceptibility gradients by inflating the endorectal coil with a barium sulfate suspension," *Magn. Reson. Med.*, vol. 57, no. 5, pp. 898–904, 2007.

[66] G. Groenendaal, C. A. van den Berg, J. G. Korporaal, M. E. Philippens, P. R. Luijten, M. van Vulpen, and U. A. van der Heide, "Simultaneous MRI diffusion and perfusion imaging for tumor delineation in prostate cancer patients," *Radiother. Oncol.*, vol. 95, no. 2, pp. 185–190, 2010.

[67] G. M. Villeirs, K. L Verstraete, W. J. De Neve, and G. O. De Meerleer, "Magnetic resonance imaging anatomy of the prostate and periprostatic area: a guide for radiotherapists," *Radiother. Oncol.*, vol. 76, no. 1, pp. 99–106, 2005.

[68] G. M. Villeirs and G. O. De Meerleer, "Magnetic resonance imaging (MRI) anatomy of the prostate and application of MRI in radiotherapy planning.," *Eur. J. Radiol.*, vol. 63, pp. 361–8, 2007.

[69] E. Yacoub, A. Shmuel, J. Pfeuffer, V. De Moortele, G. Adriany, P. Andersen, J. T. Vaughan, H. Merkle, K. Ugurbil, and X. Hu, "Imaging brain function in humans at 7 Tesla," *Magn. Reson. Med.*, vol. 45, no. 4, pp. 588–594, 2001.

[70] W. Liu, B. Turkbey, J. Sénégas, S. Remmele, S. Xu, J. Kruecker, M. Bernardo, B. J. Wood, P. A. Pinto, and P. L. Choyke, "Accelerated T2 mapping for characterization of prostate cancer," *Magn. Reson. Med.*, vol. 65, no. 5, pp. 1400–1406, 2011.

[71] P. Gibbs, G. P. Liney, M. D. Pickles, B. Zelhof, G. Rodrigues, and L. W. Turnbull, "Correlation of ADC and T2 measurements with cell density in prostate cancer at 3.0 Tesla," *Invest. Radiol.*, vol. 44, no. 9, pp. 572–576, 2009.

[72] A. Borren, G. Groenendaal, P. Van der Groep, M. R. Moman, A. E. Boeken Kruger, U. A. Van Der Heide, T. N. Jonges, P. J. Van Diest, M. Van Vulpen, and M. E. Philippens, "Expression of hypoxia-inducible factor-1α and-2α in whole-mount prostate histology: Relation with dynamic contrast-enhanced mri and gleason score," *Oncol. Rep.*, vol. 29, no. 6, pp. 2249–2254, 2013.

[73] H. Ragnum, L. Vlatkovic, A. Lie, K. Axcrona, C. Julin, K. Frikstad, K. Hole, T. Seierstad, and H. Lyng, "The tumour hypoxia marker pimonidazole reflects a transcriptional programme associated with aggressive prostate cancer," *Br. J. Cancer*, vol. 112, no. 2, pp. 382–390, 2015.

[74] M. R. Ambrosio, C. Di Serio, G. Danza, B. J. Rocca, A. Ginori, I. Prudovsky, N. Marchionni, M. T. del Vecchio, and F. Tarantini, "Carbonic anhydrase ix is a marker of hypoxia and correlates with higher gleason scores and isup grading in prostate cancer," *Diagnostic Pathol.*, vol. 11, no. 1, p. 45, 2016.

[75] S. Posse, Z. Shen, V. Kiselev, and L. J. Kemna, "Single-shot t2* mapping with 3d compensation of local susceptibility gradients in multiple regions," *Neuroimage*, vol. 18, no. 2, pp. 390–400, 2003.

[76] K.-J. Jung, H. Peng, T. Zhao, G. Avidan, and M. Behrmann, "Recovery of signal loss due to an in-plane susceptibility gradient in the gradient echo EPI through acquisition of extended phase-encoding lines," *Magn. Reson. Imaging*, vol. 28, no. 6, pp. 777–783, 2010.

[77] M. A. Fernandez-Seara and F. W. Wehrli, "Postprocessing technique to correct for background gradients in image-based R*(2) measurements," *Magn. Reson. Med.*, vol. 44, no. 3, pp. 358–66, 2000.

[78] X. Yang, S. Sammet, P. Schmalbrock, and M. V. Knopp, "Postprocessing correction for distortions in T2* decay caused by quadratic cross-slice B0 inhomogeneity," *Magn. Reson. Med.*, vol. 63, no. 5, pp. 1258–68, 2010.

[79] P. A. Ciris, M. Balasubramanian, R. T. Seethamraju, J. Tokuda, J. Scalera, T. Penzkofer, F. M. Fennessy, C. M. Tempany-Afdhal, K. Tuncali, and R. V. Mulkern, "Characterization of gradient echo signal decays in healthy and cancerous prostate at 3t improves with a gaussian augmentation of the mono-exponential (game) model," *NMR in Biomed.*, vol. 29, no. 7, pp. 999–1009, 2016.

[80] H. de Leeuw and C. J. G. Bakker, "Correction of gradient echo images for first and second order macroscopic signal dephasing using phase derivative mapping.," *Neuroimage*, vol. 60, pp. 818–29, 2012.

[81] I. N. Fleming, R. Manavaki, P. J. Blower, C. West, K. J. Williams, A. L. Harris, J. Domarkas, S. Lord, C. Baldry, and F. J. Gilbert, "Imaging tumour hypoxia with positron emission tomography," *Br. J. Cancer*, vol. 112, no. 2, pp. 238–250, 2015.

[82] C. Baudelet and B. Gallez, "How does blood oxygen level-dependent (bold) contrast correlate with oxygen partial pressure (po2) inside tumors?," *Magn. Reson. Med.*, vol. 48, no. 6, pp. 980–986, 2002.

[83] D. Zhao, L. Jiang, E. W. Hahn, and R. P. Mason, "Comparison of 1h blood oxygen level–dependent (bold) and 19f mri to investigate tumor oxygenation," *Magn. Reson. Med.*, vol. 62, no. 2, pp. 357–364, 2009.

[84] R. R. Hallac, H. Zhou, R. Pidikiti, K. Song, S. Stojadinovic, D. Zhao, T. Solberg, P. Peschke, and R. P. Mason, "Correlations of noninvasive bold and told mri with po2 and relevance to tumor radiation response," *Magn. Reson. Med.*, vol. 71, no. 5, pp. 1863–1873, 2014.

[85] A. Cheikh, N. Girouin, M. Colombel, J.-M. Maréchal, A. Gelet, A. Bissery, M. Rabilloud, D. Lyonnet, and O. Rouvière, "Evaluation of T2-weighted and dynamic contrast-enhanced MRI in localizing prostate cancer before repeat biopsy," *Eur. Radiol.*, vol. 19, no. 3, pp. 770–778, 2009.

[86] M. A. Thomas, P. Narayan, J. Kurhanewicz, P. Jajodia, and M. W. Weiner, "1h MR spectroscopy of normal and malignant human prostates in Vivo," *J. Magn. Reson. (1969)*, vol. 87, no. 3, pp. 610–619, 1990.

[87] J. Kurhanewicz, D. B. Vigneron, S. J. Nelson, H. Hricak, J. M. MacDonald, B. Konety, and P. Narayan, "Citrate as an in vivo marker to discriminate prostate cancer from benign prostatic hyperplasia and normal prostate peripheral zone: detection via localized proton spectroscopy.," *Urology*, vol. 45, pp. 459–66, 1995.

[88] A. Heerschap, M. Graaf, J. Barentsz, J. d. l. Rosette, G. Oosterhof, T. Ruijter, and S. Ruijs, "In vivo proton MR spectroscopy reveals altered metabolite content in malignant prostate tissue," *Anticancer Res.*, vol. 17, no. 3A, pp. 1455–1460, 1997.

[89] M. L. García-Martín, M. Adrados, M. P. Ortega, I. Fernández González, P. López-Larrubia, J. Viaño, and J. M. García-Segura, "Quantitative (1) H MR spectroscopic imaging of the prostate gland using LCModel and a dedicated basis-set: correlation with histologic findings.," *Magn. Reson. Med.*, vol. 65, pp. 329–39, 2011.

[90] M. G. Swanson, A. S. Zektzer, Z. L. Tabatabai, J. Simko, S. Jarso, K. R. Keshari, L. Schmitt, P. R. Carroll, K. Shinohara, D. B. Vigneron, and J. Kurhanewicz, "Quantitative analysis of prostate metabolites using 1h HR-MAS spectroscopy," *Magn. Reson. Med.*, vol. 55, no. 6, pp. 1257–1264, 2006.

[91] G. F. Giskeødegård, H. Bertilsson, K. M. Selnæs, A. J. Wright, T. F. Bathen, T. Viset, J. Halgunset, A. Angelsen, I. S. Gribbestad, and M.-B. Tessem, "Spermine and Citrate as Metabolic Biomarkers for Assessing Prostate Cancer Aggressiveness," *PLoS One*, vol. 8, no. 4, p. e62375, 2013.

[92] J. Garcia-Segura, M. Sanchez-Chapado, C. Ibarburen, J. Viano, J. Angulo, J. Gonzalez, and J. Rodriguez-Vallejo, "In vivo proton magnetic resonance spectroscopy of diseased prostate: spectroscopic features of malignant versus benign pathology," *Magn. Reson. Imaging*, vol. 17, no. 5, pp. 755–765, 1999.

[93] M. J. Lynch and J. K. Nicholson, "Proton MRS of human prostatic fluid: Correlations between citrate, spermine, and myo-inositol levels and changes with disease," *Prostate*, vol. 30, no. 4, pp. 248–255, 1997.

[94] N. J. Serkova, E. J. Gamito, R. H. Jones, C. O'Donnell, J. L. Brown, S. Green, H. Sullivan, T. Hedlund, and E. D. Crawford, "The metabolites citrate, myo-inositol, and spermine are potential age-independent markers of prostate cancer in human expressed prostatic secretions.," *Prostate*, vol. 68, pp. 620–8, 2008.

[95] K. Stenman, P. Stattin, H. Stenlund, K. Riklund, G. Gröbner, and A. Bergh, "H HRMAS NMR Derived Bio-markers Related to Tumor Grade, Tumor Cell Fraction, and Cell Proliferation in Prostate Tissue Samples.," *Biomarker Insights*, vol. 6, pp. 39–47, 2011.

[96] D. W. J. Klomp, A. K. Bitz, A. Heerschap, and T. W. J. Scheenen, "Proton spectroscopic imaging of the human prostate at 7 T," *NMR Biomed.*, vol. 22, no. 5, pp. 495–501, 2009.

[97] D. W. J. Klomp, B. L. van de Bank, A. Raaijmakers, M. A. Korteweg, C. Possanzini, V. O. Boer, C. A. T. van de Berg, M. van de Bosch, and P. R. Luijten, "31p MRSI and 1h MRS at 7 T: initial results in human breast cancer," *NMR Biomed.*, 2011.

[98] C. S. Arteaga de Castro, M. P. Luttje, M. van Vulpen, P. R. Luijten, U. A. van der Heide, and D. W. Klomp, "Composite slice-selective adiabatic excitation for prostate MRSI," *NMR Biomed.*, 2012.

[99] M. Basharat, M. Jafar, N. M. deSouza, and G. S. Payne, "Evaluation of short-TE 1h MRSI for quantification of metabolites in the prostate," *NMR Biomed.*, vol. 27, no. 4, pp. 459–467, 2014.

[100] M. Basharat, G. S. Payne, V. A. Morgan, C. Parker, D. Dearnaley, and N. M. deSouza, "TE= 32 ms vs TE= 100 ms echo-time 1h-magnetic resonance spectroscopy in prostate cancer: Tumor metabolite depiction and absolute concentrations in tumors and adjacent tissues," *J. Magn. Reson. Imaging*, vol. 42, no. 4, pp. 1086–1093, 2015.

[101] N. Venugopal, B. McCurdy, S. Al Mehairi, A. Alamri, G. S. Sandhu, S. Sivalingam, D. Drachenberg, and L. Ryner, "Short echo time in vivo prostate ^{1}H-MRSI.," *Magn. Reson. Imaging*, vol. 30, pp. 195–204, 2012.

[102] M. Mescher, A. Tannus, M. Johnson, and M. Garwood, "Solvent suppression using selective echo dephasing," *Journal of Magnetic Resonance, Series A*, vol. 123, no. 2, pp. 226–229, 1996.

[103] M. Mescher, H. Merkle, J. Kirsch, M. Garwood, and R. Gruetter, "Simultaneous in vivo spectral editing and water suppression," *NMR Biomed.*, vol. 11, pp. 266–272, 1998.

[104] R. A. de Graaf, G. M. Chowdhury, and K. L. Behar, "Quantification of high-resolution 1h NMR spectra from rat brain extracts," *Anal. Chem.*, vol. 83, no. 1, pp. 216–224, 2010.

[105] M. van der Graaf, R. G. Schipper, G. O. Oosterhof, J. A. Schalken, A. A. Verhofstad, and A. Heerschap, "Proton MR spectroscopy of prostatic tissue focused on the etection of spermine, a possible biomarker of malignant behavior in prostate cancer," *Magn. Reson. Mater. Phys., Biol. Med.*, vol. 10, no. 3, pp. 153–159, 2000.

[106] S. Posse, S. R. Dager, T. L. Richards, C. Yuan, R. Ogg, A. A. Artru, H.-W. Müller-Gärtner, and C. Hayes, "In vivo measurement of regional brain metabolic response to hyperventilation using magnetic resonance: Proton echo planar spectroscopic imaging (PEPSI)," *Magn. Reson. Med.*, vol. 37, pp. 858–865, 1997.

[107] J. P. Radtke, C. Schwab, M. B. Wolf, M. T. Freitag, C. D. Alt, C. Kesch, I. V. Popeneciu, C. Huettenbrink, C. Gasch, and T. Klein, "Multiparametric magnetic resonance imaging (MRI) and MRI–transrectal ultrasound fusion biopsy for index tumor detection: correlation with radical prostatectomy specimen," *Eur. Urol.*, 2016.

[108] M. R. Pokorny, M. De Rooij, E. Duncan, F. H. Schröder, R. Parkinson, J. O. Barentsz, and L. C. Thompson, "Prospective study of diagnostic accuracy comparing prostate cancer detection by transrectal ultrasound–guided biopsy versus magnetic resonance (MR) imaging with subsequent MR-guided biopsy in men without previous prostate biopsies," *Eur. Urol.*, vol. 66, no. 1, pp. 22–29, 2014.

[109] K. M. Selnæs, I. S. Gribbestad, H. Bertilsson, A. Wright, A. Angelsen, A. Heerschap, and M. Tessem, "Spatially matched in vivo and ex vivo MR metabolic profiles of prostate cancer–investigation of a correlation with Gleason score," *NMR Biomed.*, vol. 26, no. 5, pp. 600–606, 2013.

[110] L. Dickinson, H. U. Ahmed, C. Allen, J. O. Barentsz, B. Carey, J. J. Futterer, S. W. Heijmink, P. Hoskin, A. P. Kirkham, A. R. Padhani, *et al.*, "Scoring systems used for the interpretation and reporting of multiparametric mri for prostate cancer detection, localization, and characterization: could standardization lead to improved utilization of imaging within the diagnostic pathway?," *J. Magn. Res. Im.*, vol. 37, no. 1, pp. 48–58, 2013.

[111] K. R. Keshari, H. Tsachres, R. Iman, L. Delos Santos, Z. L. Tabatabai, K. Shinohara, D. B. Vigneron, and J. Kurhanewicz, "Correlation of phospholipid metabolites with prostate cancer pathologic grade, proliferative status and surgical stage - impact of tissue environment.," *NMR Biomed.*, vol. 24, pp. 691–9, 2011.

[112] T. Kobus, A. K. Bitz, M. J. van Uden, M. W. Lagemaat, E. Rothgang, S. Orzada, A. Heerschap, and T. W. Scheenen, "In vivo 31p MR spectroscopic imaging of the human prostate at 7 T: safety and feasibility," *Magn. Reson. Med.*, vol. 68, no. 6, pp. 1683–1695, 2012.

[113] D. W. J. Klomp, W. K. J. Renema, M. van der Graaf, B. E. de Galan, a. P. M. Kentgens, and a. Heerschap, "Sensitivity-enhanced 13c MR spectroscopy of the human brain at 3 Tesla.," *Magn. Reson. Med.*, vol. 55, pp. 271–8, 2006.

[114] I. M. van Kalleveen, W. Koning, V. O. Boer, P. R. Luijten, J. J. Zwanenburg, and D. W. Klomp, "Adiabatic turbo spin echo in human applications at 7 T," *Magn. Reson. Med.*, vol. 68, no. 2, pp. 580–587, 2012.

[115] J. J. Fütterer, S. W. Heijmink, T. W. Scheenen, G. J. Jager, C. A. Hulsbergen–Van de Kaa, J. A. Witjes, and J. O. Barentsz, "Prostate Cancer: Local Staging at 3-T Endorectal MR Imaging—Early Experience 1," *Radiology*, vol. 238, no. 1, pp. 184–191, 2006.

[116] J. J. Fütterer, A. Briganti, P. De Visschere, M. Emberton, G. Giannarini, A. Kirkham, S. S. Taneja, H. Thoeny, G. Villeirs, and A. Villers, "Can Clinically Significant Prostate Cancer Be Detected with Multiparametric Magnetic Resonance Imaging? A Systematic Review of the Literature," *Eur. Urol.*, vol. 68, no. 6, pp. 1045–1053, 2015.

[117] M. W. Lagemaat and T. W. Scheenen, "Role of high-field MR in studies of localized prostate cancer," *NMR Biomed.*, 2013.

[118] C. Arteaga de Castro, V. Boer, M. Luttje, T. Velden, A. Bhogal, M. Vulpen, P. Luijten, U. Heide, and D. Klomp, "Temporal B0 field variation effects on MRSI of the human prostate at 7 T and feasibility of correction using an internal field probe," *NMR Biomed.*, vol. 27, no. 11, pp. 1353–1360, 2014.

[119] W. J. M. van der Kemp, V. O. Boer, P. R. Luijten, J. P. Wijnen, and D. W. J. Klomp, "Increase in SNR for 31p MR spectroscopy by combining polarization transfer with a direct detection sequence.," *Magn. Res. Med.*, vol. 68, pp. 353–7, 2012.

[120] M. W. Lagemaat, M. C. Maas, E. K. Vos, A. K. Bitz, S. Orzada, E. Weiland, M. J. Uden, T. Kobus, A. Heerschap, and T. W. Scheenen, "31p MR spectroscopic imaging of the human prostate at 7 T: T1 relaxation times, Nuclear Overhauser Effect, and spectral characterization," *Magn. Reson. Med.*, vol. 73, no. 3, pp. 909–920, 2015.

[121] W. Kemp, V. Boer, P. Luijten, B. Stehouwer, W. Veldhuis, and D. Klomp, "Adiabatic multi-echo 31p spectroscopic imaging (AMESING) at 7 T for the measurement of transverse relaxation times and regaining of sensitivity in tissues with short T2* values," *NMR Biomed.*, vol. 26, no. 10, pp. 1299–1307, 2013.